nature chemical biology

ARTICLES

https://doi.org/10.1038/s41589-018-0044-1

Corrected: Publisher Correction

Direct multiplex imaging and optogenetics of Rho GTPases enabled by near-infrared FRET

Daria M. Shcherbakova[1,2], Natasha Cox Cammer[1], Tsipora M. Huisman[1], Vladislav V. Verkhusha[1,2,3]* and Louis Hodgson[1,2]*

Direct visualization and light control of several cellular processes is a challenge, owing to the spectral overlap of available genetically encoded probes. Here we report the most red-shifted monomeric near-infrared (NIR) fluorescent protein, miRFP720, and the fully NIR Förster resonance energy transfer (FRET) pair miRFP670–miRFP720, which together enabled design of biosensors compatible with CFP–YFP imaging and blue-green optogenetic tools. We developed a NIR biosensor for Rac1 GTPase and demonstrated its use in multiplexed imaging and light control of Rho GTPase signaling pathways. Specifically, we combined the Rac1 biosensor with CFP–YFP FRET biosensors for RhoA and for Rac1–GDI binding, and concurrently used the LOV-TRAP tool for upstream Rac1 activation. We directly observed and quantified antagonism between RhoA and Rac1 dependent on the RhoA-downstream effector ROCK; showed that Rac1 activity and GDI binding closely depend on the spatiotemporal coordination between these two molecules; and simultaneously observed Rac1 activity during optogenetic manipulation of Rac1.

Multiplexing of fluorescent biosensors and optogenetic systems in live-cell imaging requires spectrally compatible imaging probes. Previously, FRET biosensors based on cyan fluorescent protein (CFP) and yellow fluorescent protein (YFP) of the green fluorescent protein (GFP)-like family have been multiplexed with cellular reporters based on NIR organic dyes[1,2] and with FRET biosensors with orange and red fluorescent proteins (FPs), which require specialized imaging methods because of their substantial spectral overlap with the CFP–YFP pair[3–6]. CFP–YFP biosensors also cannot be used simultaneously with many optogenetic tools, including light-oxygen-voltage (LOV), cryptochrome-2 and channelrhodopsins[7,8], all of which are activated with blue–green light. Several NIR FPs have been developed[9]. However, these spectrally resolvable NIR fluorescent proteins (iRFPs) are dimers, a characteristic limiting their use in FRET biosensors. Recently, three monomeric iRFPs (miRFPs) have been reported[10], but the most blue-shifted and red-shifted monomeric NIR FPs do not yield efficient FRET pairs, because of their substantial spectral cross-talk. To achieve better FRET compatibility, a more red-shifted monomeric NIR FP is required.

FRET biosensors for Rho GTPases have been instrumental in studying this important class of signaling proteins. Rho GTPases are molecular switches[11] that are activated by the release of GDP and the loading of GTP, a process catalyzed by upstream regulator G-nucleotide exchange factors (GEFs)[12]. When on, Rho GTPases bind their effectors and propagate signals regulating cellular functions. Binding to GTPase-activating protein (GAP) accelerates the hydrolysis of GTP to GDP, thereby turning off the GTPases. The G-nucleotide dissociation inhibitors (GDIs) are negative regulators that bind and chaperone Rho GTPases away into the cytosol[13]. Understanding the molecular regulation of Rho GTPases is clearly important because their roles are critical both in normal cellular functions and in many diseases[14]. Importantly, Rho GTPases exist in coordinated signaling networks with rapid spatiotemporal dynamics[1]. To better understand such coordination, new NIR-FRET pairs of FPs are required that enable simultaneous probing of multiple processes and provide the ability to perturb and simultaneously observe different Rho GTPase pathways in a cell.

Here we describe the most red-shifted monomeric NIR FP to date, miRFP720. In mammalian cells, miRFP720 is the brightest among the available monomeric NIR FPs developed from bacterial phytochromes. We demonstrated the use of miRFP720 in various expression tags and characterized it as an effective FRET acceptor for the previously described blue-shifted NIR FP miRFP670 (ref. [10]), thus yielding what is, to our knowledge, the first fully NIR FRET pair. Using this pair, we engineered a genetically encoded, single-chain, monomeric NIR-FRET biosensor for Rac1 GTPase with excellent brightness and signal dynamic range. We multiplexed the NIR Rac1 biosensor with several CFP–YFP FRET biosensors and with a LOV-based optogenetic tool for simultaneous detection and perturbation of Rho GTPase activity in single living cells. First, with the NIR Rac1 biosensor and a CFP–YFP RhoA biosensor[15], we directly visualized a Rac1–RhoA antagonism in motile cells, which was dependent on the RhoA–ROCK pathway. Second, with the NIR Rac1 biosensor and a CFP–YFP biosensor for Rac1–GDI binding[2], we found a tight spatiotemporal regulation of Rac1 and observed a previously undescribed coexistence of activated Rac1 and GDI-bound Rac1 in specific cellular regions within edge protrusions. We then modified the LOV-TRAP optogenetic tool[16] to achieve higher Rac1 specificity and demonstrated the ability of the NIR Rac1 biosensor to continuously measure Rac1 activity during photoactivation followed by dark relaxation. Finally, we extended the NIR technology to kinase biosensors targeting protein kinase A (PKA) and c-Jun N-terminal kinase (JNK). We demonstrated that this NIR-FRET pair of FPs is generally applicable to biosensor development and is highly compatible with existing CFP–YFP biosensors and blue–green optogenetic tools.

Results

Engineering and characterization of miRFP720. To develop a monomeric NIR FP-based FRET acceptor, we turned to the most

---

[1]Department of Anatomy and Structural Biology, Albert Einstein College of Medicine, Bronx, NY, USA. [2]Gruss-Lipper Biophotonics Center, Albert Einstein College of Medicine, Bronx, NY, USA. [3]Department of Biochemistry and Developmental Biology, Faculty of Medicine, University of Helsinki, Helsinki, Finland. *e-mail: vladislav.verkhusha@einstein.yu.edu; louis.hodgson@einstein.yu.edu

NIR-shifted dimeric FP, iRFP720, engineered from the PAS–GAF domains of the RpBphP2 bacterial phytochrome[9]. Because the crystal structure of iRFP720 has not yet been determined, we analyzed the structure of the PAS–GAF domains of RpBphP2 (ref. [17]). These domains were crystallized as a dimer with a dimerization interface formed by the C-terminal helices of both GAF domains. Specifically, amino acid residues L309, Q312, V313 and W316 (Supplementary Results, Supplementary Fig. 1; the subsequent residue numbering follows that in Supplementary Fig. 1) formed hydrophobic interactions with their counterparts in the other protomer. Importantly, the C-terminal helices of the GAF domains were the same in RpBphP2 and iRFP720 and probably formed the dimerization interface in iRFP720. To introduce amino acid substitutions into the interface, we considered amino acids at the C termini of recently reported monomeric miRFPs developed from different bacterial RpBphP1 phytochromes. We hypothesized that substituting the five amino acid residues in the putative dimerization interface of iRFP720 with charged residues[10] should yield a monomeric iRFP720 (Supplementary Fig. 1). The resultant iRFP720 E308K L309R Q312E V313R W316T mutant was brightly fluorescent and had an absorbance maximum at 702 nm and an emission maximum at 720 nm (Supplementary Table 1 and Supplementary Fig. 2a,b). These maxima are the most NIR shifted among currently available monomeric NIR FPs (Fig. 1a,b). Further comparison of this mutant with parental iRFP720 and miRFP670 (ref. [10]) through analytical ultracentrifugation confirmed its monomeric state (Supplementary Fig. 3). We termed this mutant miRFP720 and determined that its extinction coefficient is 98,000 M^{-1} cm^{-1}, its quantum yield is 6.1%, and its pK_a value is 4.5 (Supplementary Table 1 and Supplementary Fig. 2c). As expected, monomerization did not change the properties of miRFP720 compared with those of parental iRFP720 (Supplementary Table 1), because the introduced mutations were at the C terminus of the protein, distant from the chromophore pocket (Supplementary Fig. 1).

We expressed miRFP720 in HeLa cells and compared its cellular brightness against that of other miRFPs and parental iRFP720 (Fig. 1c). The brightness of cytoplasmic miRFP720 was 1.6-fold higher than that of cells expressing miRFP670 and 3.9-fold higher than that of cells expressing miRFP709 (ref. [10]). This result indicated that miRFP720 retains a high efficiency of binding to the biliverdin (BV) chromophore in mammalian cells, a property characteristic of the parental iRFP720 (ref. [9]). In cells, miRFP720 was as bright as iRFP720 (Fig. 1c). The photostability of miRFP720 in living cells was high and similar to that of previously reported miRFPs (Supplementary Table 1 and Supplementary Fig. 2d). To test the performance of miRFP720 as a protein tag, we expressed several fusions in mammalian cells. Both N- and C-terminal fusions localized properly, including with histone 2B, which localized appropriately through mitosis and did not affect cell division (Supplementary Fig. 4).

Its high extinction coefficient and NIR-shifted excitation and emission spectra make miRFP720, as compared with other miRFPs, an advantageous FRET acceptor for a blue-shifted miRFP670 FRET donor (Supplementary Fig. 5a,b). Importantly, the red-shifted excitation spectrum of miRFP720 resulted in minimal direct cross-excitation of this FP in a FRET pair (Supplementary Fig. 5a,b). To test the FRET efficiency of this FP pair, we made a miRFP670–miRFP720 fusion connected by a linker containing the caspase-3–cleavage site -DEVD- and compared its FRET changes after induction of apoptosis with those of the miRFP670 fusion with miRFP709 (Supplementary Fig. 5c). In transiently transfected HeLa cells, the miRFP670–miRFP720 FRET pair demonstrated a 34% change in the donor/FRET ratio after caspase-3 cleavage, whereas the miRFP670–miRFP709 FRET pair resulted in a donor/FRET ratio of 18%, approximately half that of the miRFP670–miRFP720 FRET pair (Supplementary Fig. 5d,e). This result indicated the superiority of miRFP720 as a FRET acceptor over miRFP709. To compare the miRFP670–miRFP720 FRET pair with standard FRET pairs consisting of GFP-like FPs, we calculated its Förster radius (R_0). The calculated R_0 of 8.3 nm for the miRFP670–miRFP720 FRET pair was 1.5 to 1.7 times that of the standard GFP-like FRET pairs, such as CFP–YFP ($R_0 = 4.9$ nm) or mCerulean–mVenus ($R_0 = 5.4$ nm)[18], thus suggesting that substantially longer linkers between FPs and sensing parts may be required to design optimal NIR-FRET biosensors. The larger R_0 for the miRFP670–miRFP720 FRET pair should also lead to higher FRET efficiency in constructs with similar linkers. The main reason for the similar FRET efficiencies experimentally observed in the NIR-FRET pair (Supplementary Fig. 5d) and GFP-like FRET pair[19] is direct cross-excitation of the acceptor. Compared with GFP-like FPs, NIR FPs have wider spectra that lead to this effect.

NIR Rac1 FRET biosensor using miRFP670–miRFP720. Using the new miRFP670–miRFP720 FRET pair, we developed a monomeric, single-chain biosensor for Rac1 GTPase. We chose Rac1 because it has well-recognized roles in Rho GTPase signaling that are important in regulating many cellular behaviors. The wide availability of biosensors and optogenetic tools for detecting Rho GTPases through blue–green–yellow fluorescence should enable simultaneous use of the new NIR Rac1 biosensor in imaging

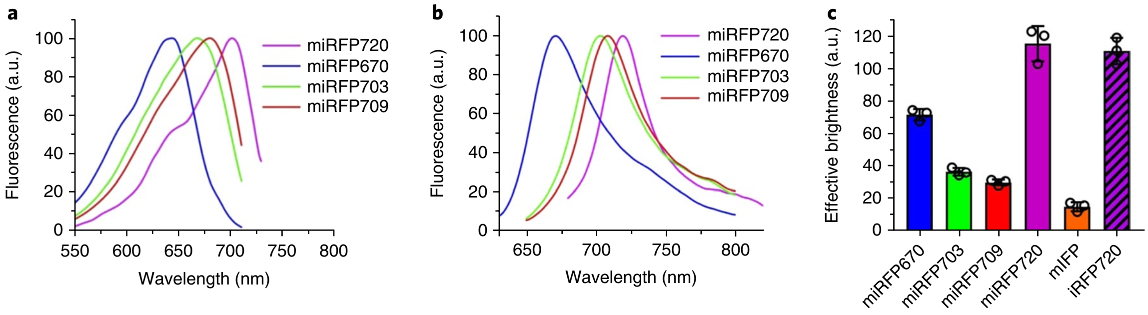

Fig. 1 | Characterization of the engineered monomeric miRFP720. a,**b** Fluorescence excitation (**a**) and emission (**b**) spectra of miRFP720 (magenta) overlaid with spectra of other monomeric NIR FPs: miRFP670 (blue), miRFP703 (green) and miRFP709 (red). **c**, NIR fluorescence brightness in live HeLa cells transiently transfected with miRFP720 (magenta, open bars) compared with parental dimeric iRFP720 (magenta, shaded bar) and other monomeric NIR FPs: miRFP670 (blue), miRFP703 (green), miRFP709 (red) and mIFP (orange), analyzed through flow cytometry. NIR fluorescence intensity was normalized to transfection efficiency (fluorescence intensity of cotransfected EGFP), to the excitation efficiency of each NIR FP with a 635-nm laser, and to the fluorescence signal of each NIR FP in the emission filter. Data are shown as mean ± s.d. ($n = 3$ independent experiments). A.u., arbitrary units.

experiments. The design of this biosensor consists of a NIR-FRET donor (miRFP670) and a NIR-FRET acceptor (miRFP720) with the p21-binding domain (PBD) of p21-activated kinase-1 (PAK1) and full-length Rac1 (Fig. 2a)[20]. In addition to miRFP720, we tested the previously reported miRFP703 and miRFP709 (ref. [10]) as FRET acceptors in several orientations within the biosensor. The optimal FRET response was observed with miRFP720 occupying the 'FP1' position and miRFP670 occupying the 'FP2' position (Supplementary Fig. 6a). To account for the larger Förster radius of this NIR-FRET pair (8.3 nm) relative to those of GFP-like FPs, we included an additional flexible linker[15] (denoted L1; Fig. 2a) and optimized for a length of 58 amino acids. At and above that length, the FRET ratios from both constitutively active and dominant-negative versions of the biosensor reached a minimum, but the differences between the two mutants were maximized at that length compared with shorter linker lengths (Supplementary Fig. 7a). A second linker of ten amino acids (denoted L2; Fig. 2a) was included (Supplementary Fig. 7b) to minimize FRET in the dominant-negative version of the biosensor. The final design of the NIR Rac1 biosensor maintained the native Rac1 C terminus and was able to interact with the upstream regulator GDI (Fig. 2b). The PBD affinity was fine-tuned through an autoinhibitory motif that optimized sensitivity[20], and the use of monomeric components minimized spurious intra- and intermolecular interactions affecting localization and reversibility.

Fluorometric characterization of the NIR Rac1 biosensor revealed a 2.7-fold difference between the on versus the off state of the biosensor (Fig. 2b). G12V or Q61L constitutively active mutants showed greater FRET than did the wild-type (WT) Rac1 biosensor, but coexpression of GDI attenuated FRET only for the WT and

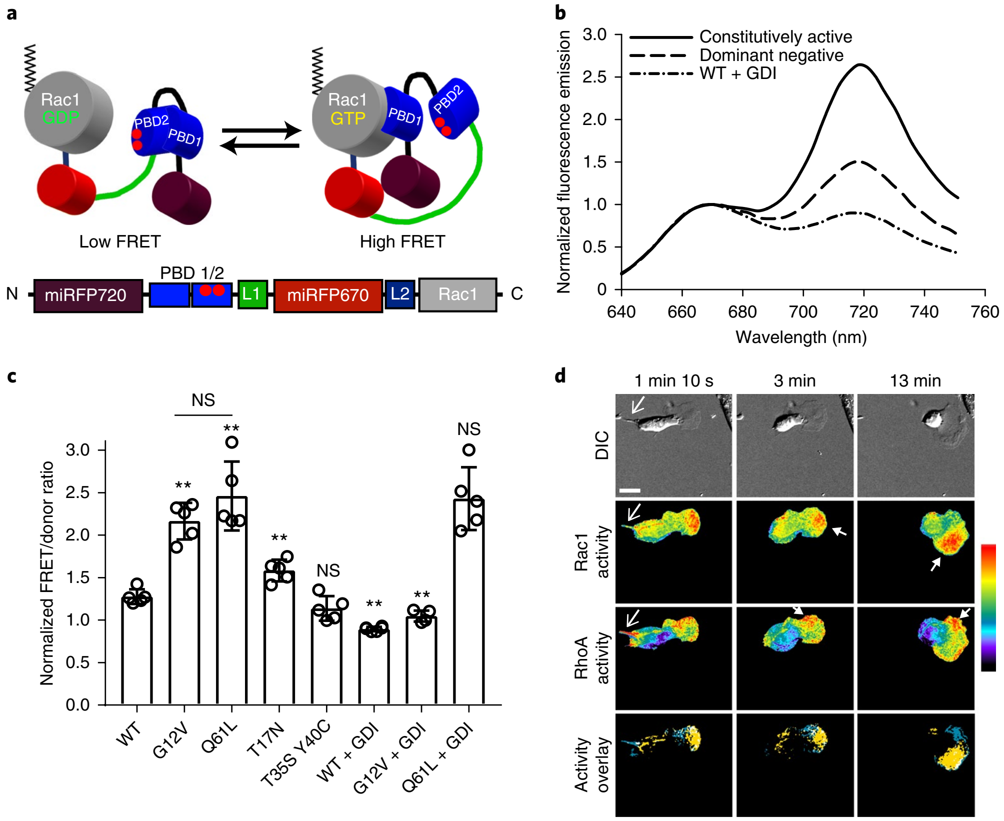

Fig. 2 | NIR Rac1 biosensor for live-cell imaging. a, Schematic of the single-chain NIR Rac1 biosensor design. From N to C terminus: dark red, miRFP720; blue, p21-binding domain 1 (PBD1) and p21-binding domain containing H83D H86D (red circles) GTPase-binding-deficient mutations (PBD2); green, linker 1; red, miRFP670; dark blue, linker 2; gray, full-length Rac1. This orientation enables post-translational isoprenylation of the C terminus, thus maintaining the native interaction with appropriate membrane domains and the GDI. GTP versus GDP loading of Rac1 changes the intramolecular conformation and affects FRET. **b**, Representative normalized fluorescence emission spectra of constitutively activated NIR Rac1 biosensor, dominant-negative NIR Rac1 biosensor and WT NIR Rac1 biosensor expressed with excess GDI. Spectra were measured by excitation of the NIR Rac1 sensor mutants expressed in cell suspensions at a 600-nm wavelength, and are from the data analyzed and presented in **c**, from 5 independent experiments. **c**, WT or mutant versions of NIR Rac1 biosensor with or without fourfold-excess GDI. Data are shown as mean ± s.e.m. ($n=5$ independent experiments). **Significant by two-tailed Student's *t* test; NS, nonsignificant. Exact *P* values: WT versus G12V, $P=2.626562\times10^{-5}$; WT versus Q61L, $P=2.158669\times10^{-4}$; WT versus T17N, $P=2.122228\times10^{-3}$; WT versus T35S Y40C, $P=0.1003134$; G12V versus Q61L, $P=0.1877456$; WT versus WT + GDI, $P=2.627320\times10^{-6}$; G12V versus G12V + GDI, $P=3.684825\times10^{-6}$; and Q61L versus Q61L + GDI, $P=0.9049651$. **d**, Representative time-lapse panels of imaging of RhoA and Rac1 in a single living MEF (additional time points in Supplementary Fig. 11) from 16 cells from 6 independent experiments. 628/32 and 436/20 excitation filters were used for NIR and mCerulean-mVenus FRET excitation, respectively. A 480/40 and 535/30 filter pair was used for the mCerulean–mVenus FRET signal, whereas a 684/24 and 794/160 filter pair was used for the miRFP670–miRFP720 FRET signal. DIC, differential interference contrast. Bottom row shows an overlay of localizations of high Rac1 (yellow) and high RhoA (blue) activities, with regions of colocalization shown in white. Regions of high Rac1 and RhoA activities were defined by intensity thresholding the top 2.5% of pixel-ratio values within the image-intensity histogram. Regions and features of interest are indicated with matching-colored arrowheads. Scale bar, 20 µm. Pseudocolor bar corresponds to ratio limits of 1.0–1.55 for Rac1 and 1.0–1.32 for RhoA activities (black to red).

G12V mutant, which bind GDI, but not for the Q61L mutant, which cannot bind GDI (Fig. 2c). The T17N dominant-negative mutant and the T35S Y40C effector-binding mutant showed attenuated FRET (Fig. 2c). Co-expression of the Rac-targeting (Trio) but not the Cdc42-targeting (Intersectin) GEFs resulted in increased FRET (Supplementary Fig. 6b). Coexpression of p50 Rho GAP attenuated FRET, whereas Rap1 GAP, which does not target Rac1, had no effect (Supplementary Fig. 6b).

To determine whether effectors of Rac1 might compete for binding to the activated NIR Rac1 biosensor[15], we performed a PBD-pulldown assay from lysates of cells expressing activated NIR Rac1 biosensor. The biosensor binds exogenous PBD only when both PBDs within the biosensor are mutated[20] such that they cannot bind to activated Rac1 (Supplementary Fig. 8a). When expressed in fibroblasts (MEF/3T3), constitutively active (Q61L) versus dominant-negative (T17N) mutant NIR Rac1 biosensors showed an approximately 40% difference in FRET (Supplementary Fig. 8b). The slightly elevated FRET in the dominant-negative (T17N) mutant is probably attributable to the formation of a stable complex of GTPase and cellular GEF[21], a complex similar to the stable complexes between GEF and other dominant-negative mutants of Rac1 (G15A and D118A)[12] and showing the same FRET levels (Supplementary Fig. 8c). We applied the synonymous codon modification to the linkers and PBD domains to prevent homologous recombination during transfection and transduction[22]. To compare the activation patterns of Rac1 in the same cell, we then overexpressed the new NIR Rac1 biosensor in MEFs together with the original Rac1 biosensor based on CFP–YFP[20,23] and performed both FRET/donor ratio and subtractive FRET-based ratiometric analyses (Supplementary Fig. 9). We thus extended the Rac1 biosensor design[20,23] to enable dynamic measurement of activity by using only NIR wavelengths above 600 nm in living cells.

Simultaneous measurement of Rac1 and RhoA activities. Rac1 and RhoA GTPases are antagonistic, as demonstrated through molecular and biochemical methods[24,25]. We decided to use the NIR Rac1 biosensor with the CFP–YFP RhoA biosensor[15] in single living cells to directly probe this antagonism in live-cell imaging. Cells are sensitive to overexpression of biosensors[15]; we therefore established stable tetracycline-inducible cells expressing both RhoA and Rac1 biosensors at levels below those affecting cellular motility (Supplementary Fig. 10; representative migrating MEF from a time-lapse experiment for RhoA–Rac1 activities in Fig. 2d, Supplementary Fig. 11 and Supplementary Video 1). Rac1 activity was predominantly localized in the lamellipodia at the front of the cell, as previously shown with another class of Rac1 biosensor[1], and RhoA activity was localized at the retracting tail, in a thin band at the leading edge, or at the side edges and at the back of the leading-edge protrusion in regions opposite from the direction of cell turning.

NIR spectra of the miRFP670–miRFP720 pair showed negligible overlap with CFP–YFP (Supplementary Fig. 12a), thus indicating clean separation of two biosensor signals. The rate of photobleaching-associated changes in the FRET/donor ratio for the NIR Rac1 biosensor was minimal over the course of a live-cell experiment, as compared with the changes for the CFP–YFP RhoA biosensor (Supplementary Fig. 12b). This result indicated that both the donor and acceptor photobleached at similar rates during imaging. We tested whether excitation of the NIR Rac1 biosensor at 436 nm (the excitation wavelength for the CFP–YFP biosensor) in addition to the 628 nm used for excitation of the NIR-FRET donor, might affect the photobleaching rate. We measured only a modest effect on the FRET/donor ratio when cells were irradiated at 436 nm in addition to 628-nm excitation (Supplementary Fig. 12b). This effect probably arose from differential excitation of miRFPs at the shorter absorption peak near 400 nm (Soret band) that is common to all phytochrome-derived NIR FPs[26] (Supplementary Fig. 12c). Thus, the new NIR-FRET biosensor is compatible with multiplex imaging and requires only minimal correction for photobleaching through previous methods[27].

For spatiotemporal quantification, we turned to morphodynamic analysis[1] to analyze the activities of RhoA and Rac1 in the same cell during edge protrusion. Morphodynamic analysis quantifies periodic cycling of cellular protrusions under steady-state conditions[1]. The leading-edge motion is extracted, and activities of RhoA and Rac1 within diffusion-limited 'measurement-window segments' at the edge and at defined distances away from the edge are quantified (Methods)[1]. We used these measurements to determine the temporal cross-correlation between RhoA and Rac1 activities. We found that the activities were strongly and negatively correlated at the leading edge (within a distance of 0–0.9 μm at the edge). This result was consistent with Rac1–RhoA antagonism and is, to our knowledge, the first direct characterization of this antagonism in the same cell (Fig. 3a). The time difference between the onset of RhoA and Rac1 activity was approximately 20 s, in agreement with the previously determined delay calculated from separate imaging of two CFP–YFP biosensors of Rac1 and RhoA[1] (representative morphodynamic maps from the leading-edge window segments in Fig. 3b; Supplementary Fig. 13a and Supplementary Videos 2 and 3). Mutually exclusive Rac1 and RhoA activities were evident during noncyclical, large protrusion–retraction of the leading edge (Fig. 3b) and in smaller oscillatory protrusions (Supplementary Fig. 13a). The negative cross-correlation between RhoA and Rac1 activities at the leading edge diminished to below significance in regions away from the edge (>0.9 μm; Fig. 3a), thus indicating a strong spatial dependence. By combining the new NIR Rac1 biosensor with a CFP–YFP RhoA biosensor[15], we were able to directly measure both Rac1 and RhoA activities at the leading edge and provide a quantitative description of the Rac1–RhoA antagonism. Next, we explored a potential mechanism by which Rac1–RhoA antagonism was established at the edge. Previously, RhoA–ROCK–myosin has been shown to balance edge protrusion, wherein this contractile pathway causes stalling of the protrusion during edge cycling[28]. The role of this pathway in modulating RhoA and Rac1 activities has previously been demonstrated with a set of CFP–YFP biosensors for RhoA and Rac1, imaged separately in different cells[28]. Therefore, we sought to directly visualize this balance in RhoA- and Rac1-driven edge protrusion by similarly decoupling the mechanism through treatment with a ROCK inhibitor (Y-27632) and directly visualizing Rac1 and RhoA activities in the same cell. In agreement with the previous model[28], the negative cross-correlation between RhoA and Rac1 activities at the edge (0–0.9 μm) changed to a positive cross-correlation when ROCK was inhibited, but the strength of the correlation was not significant (Fig. 3c). Within 0.9–1.8 μm from the edge, the RhoA and Rac1 activities were positively correlated and significant (Fig. 3c). In regions further from the edge, the trend in positive cross-correlation continued but was not significant. The change in cross-correlation between RhoA and Rac1 resulted from the concomitant activation of Rac1 and RhoA; this activation probably prevented the edge from retracting and Rac1 from being deactivated in the absence of the ROCK–myosin contractility pathway. This effect was visible in a representative set of morphodynamic maps from a cell that showed noncyclical, large protrusion–retraction: Rac1–RhoA antagonism was ablated, and the two activities overlapped (Fig. 3d and Supplementary Video 4). In small oscillatory protrusions (Supplementary Fig. 13b and Supplementary Videos 3 and 5), cyclical activation of RhoA (region 0.9–1.8 μm) continued when ROCK was inhibited, but Rac1 activity remained elevated. These observations suggested that the coordination of RhoA and Rac1 via ROCK is critical in achieving the antagonism, thus suggesting that molecular

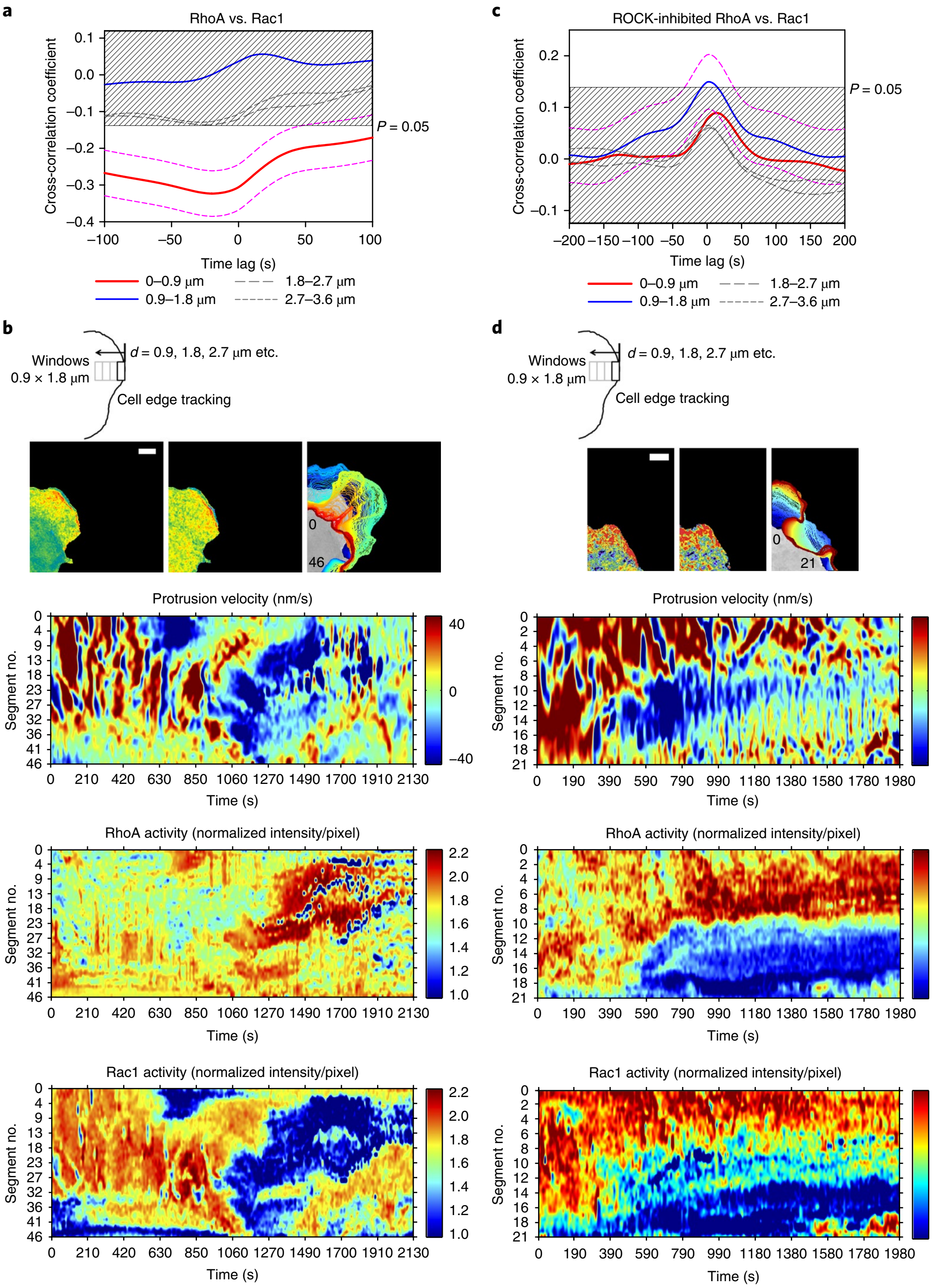

Fig. 3 | Morphodynamic analysis of RhoA–Rac1 antagonism. a, Cross-correlation coefficient as a function of time lags between RhoA and Rac1 activities at the protruding edge in MEFs. Dashed magenta lines, 95% confidence interval (95% CI) for the cross-correlation function from the edge region (red line, 0–0.9 μm). The time difference between the RhoA versus the Rac1 biosensor response was −19.6 s ± 31.6s (mean ± 95% CI); i.e., the RhoA activity onset preceded the Rac1 activity onset by approximately 19.6 s. 95% CIs are omitted from the rest of plots for clarity. The shaded region indicates $P > 0.05$ ($n = 1{,}250$ individual sampling-window segments measured from 16 cells from 6 independent experiments). **b**, Example edge-tracking evolution from a single cell (top) and associated morphodynamic maps of the velocity and RhoA and Rac1 activities (bottom three panels), from an untreated control MEF. The edge velocity, RhoA activity and Rac1 activity measured within window segments at the leading edge of a single representative cell are compiled on the *y* axes and followed over time on the *x* axes. Scale bar, 10 μm. Example set taken from total of 16 cells from 6 independent experiments. **c**, Cross-correlation coefficient as a function of time lags between RhoA and Rac1 activities at the protruding edge in MEFs treated with the ROCK inhibitor Y-27632. Dashed magenta lines indicate 95% CIs for the cross-correlation function from the region adjacent to the cell edge (blue line, 0.9–1.8 μm). 95% CIs are omitted from the rest of plots for clarity. The shaded region indicates $P > 0.05$ ($n = 990$ individual sampling-window segments measured from 18 cells from 3 independent experiments). **d**, Example edge-tracking evolution (top) from a single cell and associated morphodynamic maps of the velocity, RhoA and Rac1 activities (bottom three panels), from a MEF treated with ROCK inhibitor Y-27632. Scale bar, 10 μm. Example set taken from 18 cells from 3 independent experiments. The numbers in the edge-evolution panels in **b** and **d** (top) indicate the orientation of the measurement-window segments that correspond to the *y* axes of the morphodynamic maps as shown. Throughout figure, *P* values were determined by two-tailed Student's *t* test.

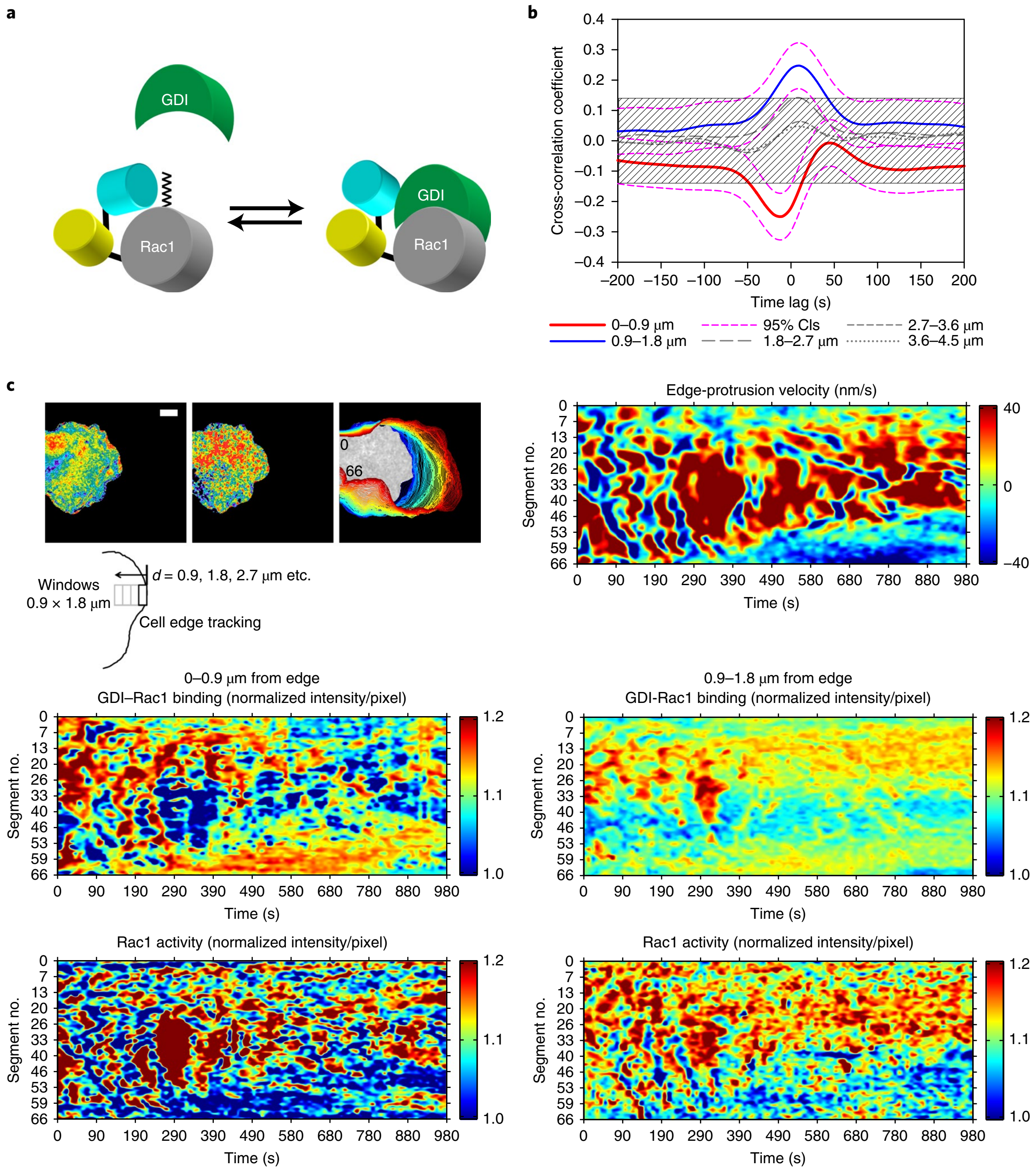

Fig. 4 | Morphodynamic analysis of Rac1 activity and Rac1–GDI binding. a, Schematic drawing of the previously reported biosensor for Rac1–GDI binding[2]. The WT Rac1 is attached to the C terminus of the FRET 'antenna' that selectively detects the binding of Rac1 to GDI. **b**, Cross-correlation coefficient as a function of time lags between Rac1–GDI binding and Rac1 activity at the protruding edge in MEFs. Dashed magenta lines, 95% CI for the cross-correlation function of the edge and the next adjacent region away from the edge (red line, 0–0.9 μm; blue line, 0.9–1.8 μm). The time differences between the Rac1–GDI versus Rac1 biosensor response was -11.9 s ± 23 s (mean ± 95% CI; the Rac1–GDI biosensor response preceded the Rac1 biosensor response) at the leading edge (red line) and +9.6 s ± 25 s (mean ± 95% CI; the Rac1 activity preceded the Rac1–GDI biosensor response) at the region adjacent to the edge (blue line). 95% CIs are omitted from the rest of plots for clarity. The shaded region indicates $P > 0.05$ ($n = 827$ individual sampling-window segments measured from 10 cells from 3 independent experiments). **c**, Example morphodynamic dataset of a MEF imaged for Rac1 activity and Rac1–GDI binding in the same cell. Shown are the edge-tracking evolution (top left) from a single cell and associated morphodynamic maps of the edge velocity (top right), Rac1–GDI binding at the edge (middle left) and at the next adjacent region away from the edge (middle right), and Rac1 activity at the edge (bottom left) and at the next adjacent region away from the edge (bottom right). Scale bar, 10 μm. Example set taken from 10 cells from 3 independent experiments. The numbers in the edge-evolution panel in **c** indicate the orientation of the measurement-window segments that correspond to the *y* axes of the morphodynamic maps as shown. Throughout figure, *P* values were determined by two-tailed Student's *t* test.

pathways regulated by ROCK may be critical in orchestrating this coordination. The ability to simultaneously detect Rac1 and RhoA activities enabled the direct observation of this phenomenon.

Multiplex imaging of Rac1 activity and Rac1–GDI binding. Regulation of Rho GTPases involves three classes of upstream regulators: GEFs, GAPs and GDIs[11]. The GDI–GTPase interaction is the

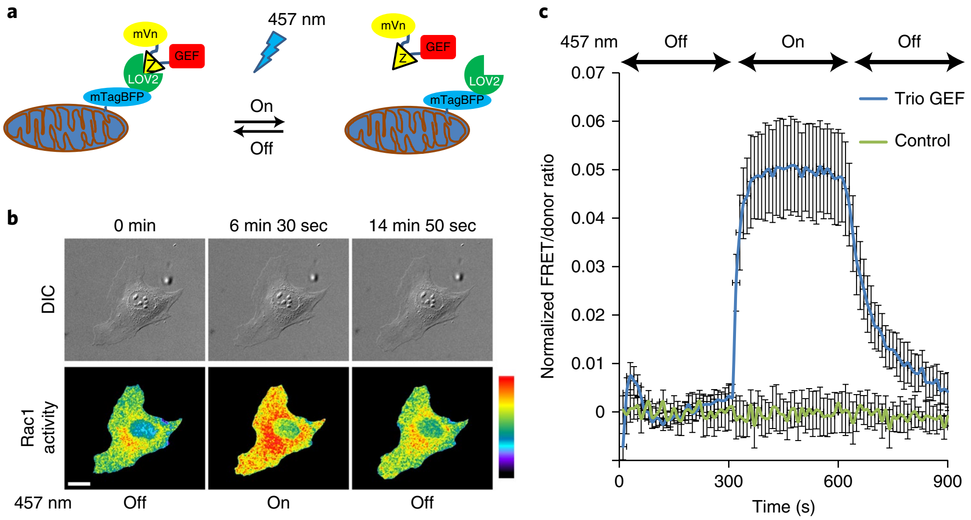

Fig. 5 | Concurrent measurement of Rac1 activity during LOV-TRAP optogenetics. a, Schematic drawing of the LOV-TRAP system. Mitochondrially targeted mtagBFP2-LOV2wt sequesters the GEF domain of interest attached to a Zdk1 molecule (Z) labeled with monomeric Venus fluorescent protein (mVn). Upon photoactivation with 457-nm light, mVn–Zdk1–GEF is released and acts on the target GTPase, and this is followed by dark relaxation after cessation of illumination. **b**, Example panel of a MEF undergoing photoactivation of LOV-TRAP and concurrent measurements of Rac1 activity with the NIR Rac1 biosensor. NIR-Rac1-biosensor image sets were acquired every 10 s. 457-nm illumination (cycles of 4 s on, 6 s off) was started at 300 s and ended at 600 s (additional time points in Supplementary Fig. 15a). Scale bar, 20 μm. Pseudocolor limits are 1.0 to 1.74 (black to red). Example taken from $n = 17$ independent photoactivation experiments. **c**, Quantification of Rac1 activity measured concurrently with LOV-TRAP–Trio GEF photoactivation. During the on phase of the 457-nm illumination, Rac1 activity levels were significantly higher than levels of the control, which received no 457-nm illumination. Two-tailed Student's *t* test was used to compare Rac1 activity during photoactivation (300–600 s) and dark relaxation (600–900 s) versus the activity before photoactivation (0–300 s), as shown in Supplementary Table 2. $n = 17$ independent photoactivation experiments for LOV-TRAP–Trio GEF; $n = 10$ independent mock-photoactivation experiments for the control condition; all data are shown as mean ± s.e.m.

least characterized among regulator interactions, but recent studies have revealed spatiotemporal dynamics, regulated in part by cellular kinases[13]. We took advantage of a recently reported CFP–YFP biosensor for Rac1–GDI binding[2] (Fig. 4a) and used it for imaging together with the NIR Rac1 biosensor in single living cells. We produced tetracycline-inducible MEFs in which both the NIR Rac1 and Rac1–GDI biosensors were stably incorporated and performed live-cell imaging and subsequent morphodynamic analysis[1]. The cross-correlation of Rac1 activity versus Rac1–GDI binding showed a high coordination at the leading edge (0–0.9 μm) and at an adjacent region away from the edge (0.9–1.8 μm), whereas distal regions were not correlated (Fig. 4b). At the edge, we observed a strongly negative and significant cross-correlation between Rac1–GDI binding versus Rac1 activation, with an approximately 12-s difference between the Rac1–GDI biosensor response and the subsequent NIR Rac1 biosensor response. This result indicated that during activation of Rac1, the release from GDI (loss of CFP–YFP FRET) was quickly followed by activation (gain of NIR FRET) in the plasma membrane, presumably through encountering a GEF (Supplementary Fig. 14). This timing is similar to that of Cdc42 activation after release from GDI[2], thus suggesting that GEF-mediated activation of GTPases occurs rapidly after the release; hence, the release from GDI may be the rate-determining step. This negative cross-correlation was visible in representative morphodynamic maps (Fig. 4c and Supplementary Video 6). Interestingly, at an adjacent region away from the edge (0.9–1.8 μm), a strongly positive and significant cross-correlation between Rac1–GDI binding and Rac1 activation was observed (Fig. 4b). This result indicated that Rac1 activates in this region at the plasma membrane but also permits binding by GDI (Supplementary Fig. 14). These results are consistent with the previous observation that activated Rac1 may be removed from signaling pathways by forming a complex with cytoplasmic GDI[29]. Use of the CFP–YFP and miRFP670–miRFP720 FRET biosensor combinations enabled the observation of a tight spatiotemporal coordination of Rac1 activation and Rac1–GDI interaction in living cells, thus revealing the complexity of spatiotemporal regulation of Rac1 by GDI.

Compatibility of the NIR Rac1 biosensor with LOV-TRAP. To demonstrate the spectral compatibility of the NIR Rac1 biosensor with optogenetics systems requiring blue–green light, including the *Avena sativa* phototropin LOV2, we decided to use the recently reported LOV-TRAP system[16] (Fig. 5a). This system consists of two components: mitochondrially targeted LOV2-Jα and the catalytic domain of a GEF fused to an affinity monobody evolved to bind reversibly to the dark state of LOV2-Jα (ref. [16]). Upon irradiation, the Jα domain becomes labile, and the monobody dissociates, thus releasing the GEF catalytic domain from mitochondrial sequestration. The released GEF domain activates Rho GTPases with a half-life of approximately 18.5 s (ref. [16]).

We modified the original LOV-TRAP to specifically target Rac1 activation by exchanging the catalytic GEF domain of Vav2, which activates RhoA, Rac1 and Cdc42, for the N-terminal DHPH-SH3 domain of Trio GEF, which targets Rac1 and another Rac family member, RhoG[30]. We produced tetracycline-inducible MEFs expressing the NIR Rac1 biosensor and transiently transfected the cells with N-TOM20-mTagBFP2-LOV2wt and mVenus-Zdk1-TrioDHPH-SH3, at a cDNA ratio of 10:1 (ref. [16]). We imaged Rac1 activity at 10-s intervals and photoactivated the LOV-TRAP at the 300-s time point with 457-nm light (cycling 4 s on/6 s off) for 300 s, which was followed by another 300 s of dark relaxation (Fig. 5b, Supplementary Fig. 15a and Supplementary Video 7). We observed rapid activation of Rac1 when LOV-TRAP was uncaged, and subsequent deactivation after cessation of photoactivation (Fig. 5c). The original LOV-TRAP containing the GEF domain of Vav2 (ref. [16]) produced Rac1 activation similar to that of Trio GEF when uncaged, but the decay in Rac1 activity during the dark relaxation appeared slower (Supplementary Fig. 15b). This finding was consistent with

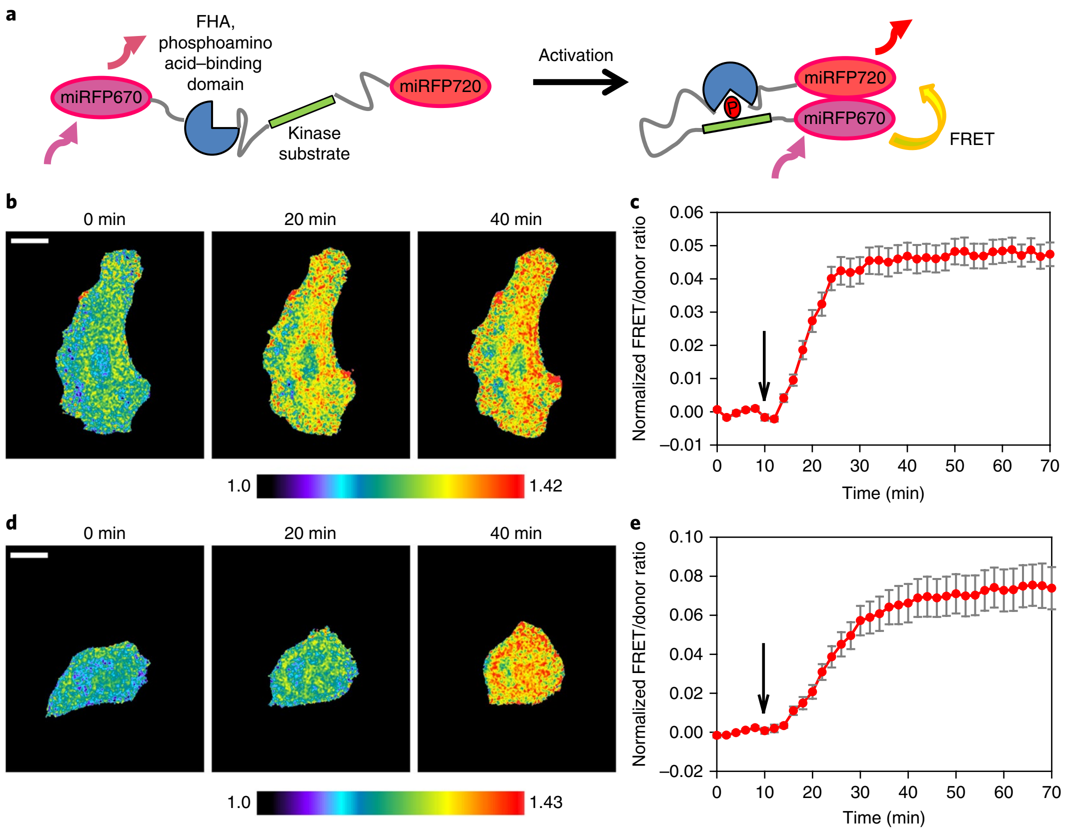

Fig. 6 | NIR-FRET pair of fluorescent proteins in kinase-substrate biosensors. a, Basic design principle for the PKA[31] and JNK[32] sensors, modified from the original CFP–YFP versions[33] to use the NIR miRFP670 (ref. [10]) and miRFP720 fluorescent proteins. **b**, Representative time-lapse images of a HeLa cell expressing the NIR AKAR PKA sensor and undergoing stimulation (additional time points in Supplementary Fig. 16a). $n=3$ independent stimulation experiments. 1 mM dibutyryl cAMP was added at the 10-min time point, and the FRET/donor ratio was monitored for up to 70 min. Scale bar, 20 μm. **c**, FRET/donor ratio from NIR AKAR, shown as mean ± s.e.m. Black arrow indicates the time point at which the stimulation was performed. $n=3$ stimulation experiments. Two-tailed Student's *t* test was used to determine *P* values between FRET/donor ratios before (0–8 min) and after (10–70 min) stimulation, as shown in Supplementary Table 3. **d**, Representative time-lapse images of a HeLa cell expressing the NIR JNKAR JNK sensor and undergoing stimulation (additional time points in Supplementary Fig. 16b). $n=3$ independent stimulation experiments. 1 μg/ml anisomycin was added at the 10-min time point, and the FRET/donor ratio was monitored for up to 70 min. Scale bar, 20 μm. **e**, FRET/donor ratio from NIR JNKAR, shown as mean ± s.e.m. Black arrow indicates the time point at which the stimulation was performed. $n=3$ independent stimulation experiments. Two-tailed Student's *t* test was used to determine *P* values between FRET/donor ratios before (0–8 min) and after stimulation (10–70 min), as shown in Supplementary Table 3.

promiscuous targeting of Vav2 toward other Rho GTPases; the cellular GAP may be limiting, or other pathways differentially controlling GTPases may have been activated. Interestingly, the LOV-TRAP did not induce changes in leading-edge movement as a function of photouncaging (or during dark relaxation), although Rac1 was activated (Supplementary Fig. 15c). This observation suggested that proper targeting of GEF, via molecular-interaction domains that either localize or facilitate assembly of the downstream-effector signaling complex within appropriate cellular compartments, is also required in addition to activated Rho GTPase to drive specific cellular phenotypes. These results demonstrated that the NIR Rac1 biosensor is complementary to, and can be used together with, common optogenetics tools controlled by blue–green-light, thus newly enabling simultaneous detection and modulation of Rho GTPase activities.

Development of NIR kinase biosensors. To demonstrate the generalizability of our new NIR-FRET pair of FPs, we extended this approach to the biosensors AKAR[31] and JNKAR[32], to detect the phosphorylation activity of the kinases PKA and JNK, respectively (Fig. 6a). We replaced the original CFP–YFP in the sensors with an optimized backbone[33] with miRFP670 and miRFP720 at the N and C termini of the sensors, and measured the cellular response to previously used stimulations[31–33] that induce phosphorylation and increases in FRET upon PKA activation (Fig. 6b,c) or JNK activation (Fig. 6d,e). Upon stimulation, the FRET/donor ratio increased rapidly and reached a plateau, as previously reported (Fig. 6c,e and Supplementary Videos 8 and 9), thus indicating that the new NIR-FRET pair of FPs reported here should be useful as a general tool to engineer genetically encoded NIR-FRET biosensors for live-cell imaging.

Discussion

From parental dimeric iRFP720, we engineered miRFP720, the most red-shifted miRFP to date. Moreover, our rationally designed site-specific amino acid substitutions in the dimerization interface of iRFP720 can be used to monomerize other dimeric NIR FPs[9]. The photochemical characteristics of miRFP720 are comparable to or better than those reported for other monomeric NIR FPs[10], thus making miRFP720 an advantageous protein tag for multicolor imaging. The red shift of miRFP720 makes it an ideal FRET acceptor when combined with miRFP670, owing to minimal cross-excitation of the acceptor and good spectral overlap between donor fluorescence and acceptor excitation. No genetically encoded NIR biosensors based on FRET had previously been available. miRFP670–miRFP720 is an efficient, fully NIR FRET pair that can be used as easily as the common CFP–YFP pair in a wide range of FRET applications. Importantly, the miRFP670–miRFP720 pair allows for multiplexing of blue–green–yellow channels of fluorescence with essentially zero spectral overlap, thus enabling cross-talk-free, simultaneous imaging with CFP–YFP biosensors[34] and modulation with blue–green optogenetic tools, such as LOV, cryptochrome-2 and channelrhodopsins[7,8].

Using the miRFP670–miRFP720 pair, we engineered a NIR biosensor for Rac1 GTPase. By combining the NIR biosensor with well-characterized and widely used CFP–YFP biosensors, we simultaneously imaged Rac1 activity with that of its antagonist RhoA, or its regulation by GDI in the same cell. Rac1–RhoA imaging revealed the antagonistic dynamic of these two canonical GTPases during cell-edge movement, a process dependent on ROCK signaling. In agreement with a previous model[28], ROCK inhibition induced robust protrusion and resulted in activation of both GTPases in the same place at the same time. This result is consistent with the idea that the RhoA–ROCK–myosin pathway acts as a braking mechanism that induces stalling of the leading edge during protrusion–retraction cycles with appropriate timing[28]. To achieve this braking, the antagonism must be established via recruitment of GEF–GAP modules that, through a feedback mechanism from the downstream molecular pathways, must be activated at the appropriate time and location. Importantly, multiplexed imaging of the dynamics of Rac1–RhoA activities suggested that Rac1 directly correlated with protrusions, and RhoA directly correlated with retractions. This finding was also consistent with measurements previously made with CFP–YFP biosensors in a different fibroblast cell line[28]. One study has shown that the onset of Rac1 occurs closer in time to the start of edge retraction, whereas that of RhoA is associated with edge protrusion[1]. This apparent difference is attributable to the different types of edge protrusions observed in our current analysis compared with previous work, as evidenced by the much longer oscillatory periodicity observed in this work (120–140 s herein versus 90 s in ref. [1]; Supplementary Fig. 10). This difference may stem from the use of different fibronectin and serum, which might have triggered differential signaling pathways[23] and changed the balance of Rac1–RhoA activities and the dynamics of protrusion. The ability to directly observe both Rac1 and RhoA activities in the same cell, as shown here, should facilitate detailed analyses of the molecular machinery that coordinates the balance of Rac1 and RhoA activities driving cell-edge protrusion.

The coordination of GTPase regulation at the leading edge was further demonstrated in our study of Rac1–GDI interaction and activation by using the NIR Rac1 biosensor in combination with the CFP–YFP Rac1–GDI biosensor[2]. Our experiments showed spatiotemporal coordination of Rac1 activation after its release from GDI at the leading edge. A positive cross-correlation observed at an adjacent region behind the leading edge indicated that activation of Rac1 was followed closely in time by binding to GDI. This result was consistent with those from previous studies indicating that GDI binds active Rac1 as a mechanism to control Rac1-effector interaction[29]. Further investigation in this area will be required to reveal the mechanism of GDI-mediated recycling and control of active Rac1 GTPase, but, to our knowledge, this is the first direct observation of such localized spatial regulation of Rac1 GTPase.

Blue–green optogenetic tools, similarly to multiplexed biosensors, have not been able to be used together with CFP–YFP biosensors. For LOV2 (ref. [16]), the CFP excitation at 440 nm is too close to the photouncaging wavelengths. In the original LOV-TRAP characterization[16], either the light or the dark mutant of the LOV-TRAP optogenetic tool was tested against CFP–YFP biosensors for Rho family GTPases[16]. Here, we demonstrated that the NIR Rac1 biosensor can be used to measure Rac1 activity at the same time as the LOV-TRAP approach[16]. The ability to monitor activity and simultaneously perturb a signaling node through optogenetics should be valuable in dissecting signal-pathway interdependency. Spectral compatibility with NIR biosensors should now enable the use of optogenetic tools in direct real-time experiments.

Finally, we demonstrated the generalizability of miRFP720 as an excellent FRET acceptor that can be coupled to miRFP670 to produce genetically encoded NIR-FRET biosensors. These biosensors allow researchers to use the NIR-FRET band for direct imaging, quantification and control of several signaling pathways in living cells. We expect these NIR-FRET probes to be suitable for use in vivo in animal-imaging modalities, because their optimal compatibility with light-absorbance characteristics in tissues enables deep tissue penetration. Combining functional imaging with noninvasive optogenetic modulation enables cell dynamics to be related to metabolic functions at the cell and tissue levels and to behavior at the organ and organismal levels.

Methods

Methods, including statements of data availability and any associated accession codes and references, are available at https://doi.org/10.1038/s41589-018-0044-1.

Received: 1 September 2017; Accepted: 1 March 2018;

References

1. Machacek, M. et al. Coordination of Rho GTPase activities during cell protrusion. *Nature* **461**, 99–103 (2009).
2. Hodgson, L. et al. FRET binding antenna reports spatiotemporal dynamics of GDI–Cdc42 GTPase interactions. *Nat. Chem. Biol.* **12**, 802–809 (2016).
3. Ouyang, M. et al. Simultaneous visualization of protumorigenic Src and MT1-MMP activities with fluorescence resonance energy transfer. *Cancer Res.* **70**, 2204–2212 (2010).
4. Grant, D. M. et al. Multiplexed FRET to image multiple signaling events in live cells. *Biophys. J.* **95**, L69–L71 (2008).
5. Demeautis, C. et al. Multiplexing PKA and ERK1&2 kinases FRET biosensors in living cells using single excitation wavelength dual colour FLIM. *Sci. Rep.* **7**, 41026 (2017).
6. Shcherbakova, D. M., Hink, M. A., Joosen, L., Gadella, T. W. & Verkhusha, V. V. An orange fluorescent protein with a large Stokes shift for single-excitation multicolor FCCS and FRET imaging. *J. Am. Chem. Soc.* **134**, 7913–7923 (2012).
7. Shcherbakova, D. M., Shemetov, A. A., Kaberniuk, A. A. & Verkhusha, V. V. Natural photoreceptors as a source of fluorescent proteins, biosensors, and optogenetic tools. *Annu. Rev. Biochem.* **84**, 519–550 (2015).
8. Chernov, K. G., Redchuk, T. A., Omelina, E. S. & Verkhusha, V. V. Near-infrared fluorescent proteins, biosensors, and optogenetic tools engineered from phytochromes. *Chem. Rev.* **117**, 6423–6446 (2017).
9. Shcherbakova, D. M. & Verkhusha, V. V. Near-infrared fluorescent proteins for multicolor in vivo imaging. *Nat. Methods* **10**, 751–754 (2013).
10. Shcherbakova, D. M. et al. Bright monomeric near-infrared fluorescent proteins as tags and biosensors for multiscale imaging. *Nat. Commun.* **7**, 12405 (2016).
11. Nobes, C. & Hall, A. Regulation and function of the Rho subfamily of small GTPases. *Curr. Opin. Genet. Dev.* **4**, 77–81 (1994).
12. García-Mata, R. & Burridge, K. Catching a GEF by its tail. *Trends Cell Biol.* **17**, 36–43 (2007).
13. Garcia-Mata, R., Boulter, E. & Burridge, K. The 'invisible hand': regulation of RHO GTPases by RHOGDIs. *Nat. Rev. Mol. Cell Biol.* **12**, 493–504 (2011).
14. Pai, S. Y., Kim, C. & Williams, D. A. Rac GTPases in human diseases. *Dis. Markers* **29**, 177–187 (2010).
15. Pertz, O., Hodgson, L., Klemke, R. L. & Hahn, K. M. Spatiotemporal dynamics of RhoA activity in migrating cells. *Nature* **440**, 1069–1072 (2006).
16. Wang, H. et al. LOVTRAP: an optogenetic system for photoinduced protein dissociation. *Nat. Methods* **13**, 755–758 (2016).
17. Bellini, D. & Papiz, M. Z. Dimerization properties of the RpBphP2 chromophore-binding domain crystallized by homologue-directed mutagenesis. *Acta Crystallogr. D Biol. Crystallogr.* **68**, 1058–1066 (2012).
18. Müller, S. M., Galliardt, H., Schneider, J., Barisas, B. G. & Seidel, T. Quantification of Förster resonance energy transfer by monitoring sensitized emission in living plant cells. *Front. Plant Sci.* **4**, 413 (2013).
19. Patterson, G. H. & Piston, D. W. Photobleaching in two-photon excitation microscopy. *Biophys. J.* **78**, 2159–2162 (2000).

20. Moshfegh, Y., Bravo-Cordero, J. J., Miskolci, V., Condeelis, J. & Hodgson, L. A Trio–Rac1–Pak1 signalling axis drives invadopodia disassembly. *Nat. Cell Biol.* **16**, 574–586 (2014).
21. Quilliam, L. A. et al. Identification of residues critical for Ras(17N) growth-inhibitory phenotype and for Ras interaction with guanine nucleotide exchange factors. *Mol. Cell. Biol.* **14**, 1113–1121 (1994).
22. Wu, B. et al. Synonymous modification results in high-fidelity gene expression of repetitive protein and nucleotide sequences. *Genes Dev.* **29**, 876–886 (2015).
23. Miskolci, V., Wu, B., Moshfegh, Y., Cox, D. & Hodgson, L. Optical tools to study the isoform-specific roles of small GTPases in immune cells. *J. Immunol.* **196**, 3479–3493 (2016).
24. Martin, E., Ouellette, M. H. & Jenna, S. Rac1/RhoA antagonism defines cell-to-cell heterogeneity during epidermal morphogenesis in nematodes. *J. Cell Biol.* **215**, 483–498 (2016).
25. Nakamura, F. FilGAP and its close relatives: a mediator of Rho-Rac antagonism that regulates cell morphology and migration. *Biochem. J.* **453**, 17–25 (2013).
26. Shcherbakova, D. M., Baloban, M. & Verkhusha, V. V. Near-infrared fluorescent proteins engineered from bacterial phytochromes. *Curr. Opin. Chem. Biol.* **27**, 52–63 (2015).
27. Hodgson, L., Nalbant, P., Shen, F. & Hahn, K. Imaging and photobleach correction of Mero-CBD, sensor of endogenous Cdc42 activation. *Methods Enzymol.* **406**, 140–156 (2006).
28. Martin, K. et al. Spatio-temporal co-ordination of RhoA, Rac1 and Cdc42 activation during prototypical edge protrusion and retraction dynamics. *Sci. Rep.* **6**, 21901 (2016).
29. del Pozo, M. A., Price, L. S., Alderson, N. B., Ren, X. D. & Schwartz, M. A. Adhesion to the extracellular matrix regulates the coupling of the small GTPase Rac to its effector PAK. *EMBO J.* **19**, 2008–2014 (2000).
30. Bellanger, J. M. et al. The two guanine nucleotide exchange factor domains of Trio link the Rac1 and the RhoA pathways in vivo. *Oncogene* **16**, 147–152 (1998).
31. Chen, Y., Saulnier, J. L., Yellen, G. & Sabatini, B. L. A PKA activity sensor for quantitative analysis of endogenous GPCR signaling via 2-photon FRET-FLIM imaging. *Front. Pharmacol.* **5**, 56 (2014).
32. Fosbrink, M., Aye-Han, N. N., Cheong, R., Levchenko, A. & Zhang, J. Visualization of JNK activity dynamics with a genetically encoded fluorescent biosensor. *Proc. Natl. Acad. Sci. USA* **107**, 5459–5464 (2010).
33. Komatsu, N. et al. Development of an optimized backbone of FRET biosensors for kinases and GTPases. *Mol. Biol. Cell* **22**, 4647–4656 (2011).
34. Piston, D. W. & Kremers, G. J. Fluorescent protein FRET: the good, the bad and the ugly. *Trends Biochem. Sci.* **32**, 407–414 (2007).

Acknowledgements

We thank M. Brenowitz (Albert Einstein College of Medicine) for help with analytical ultracentrifugation, M. Baloban (Albert Einstein College of Medicine) for help with engineering miRFP720, and O. Oliinyk (University of Helsinki) for advice on kinase biosensors. We thank S. Donnelly (Albert Einstein College of Medicine) for critical reading of the manuscript. This work was supported by grants GM122567, NS099573, and NS103573 to V.V.V., and CA205262 to L.H. from the US National Institutes of Health and ERC-2013-ADG-340233 from the EU FP7 program to V.V.V. We thank K. Aoki (Kyoto University), K. Hahn (University of North Carolina at Chapel Hill) and J. van Buul (University of Amsterdam) for providing reagents.

Author contributions

D.M.S. and V.V.V. developed the miRFP720 and characterized it in vitro, in cells and as a FRET acceptor. L.H., N.C.C. and T.M.H. engineered the NIR Rac1 biosensor, characterized it in cells and performed live-cell imaging. L.H., D.M.S. and V.V.V. designed the project, planned the experiments and discussed the data; V.V.V., D.M.S. and L.H. wrote the manuscript. All authors reviewed the manuscript.

Competing interests

The authors declare no competing interests.

Additional information

Supplementary information is available for this paper at https://doi.org/10.1038/s41589-018-0044-1.

Reprints and permissions information is available at www.nature.com/reprints.

Correspondence and requests for materials should be addressed to V.V.V. or L.H.

Publisher's note: Springer Nature remains neutral with regard to jurisdictional claims in published maps and institutional affiliations.

Methods

Cloning and protein expression. Site-specific mutagenesis of iRFP720 cloned in the pBAD/His-B vector was performed with a QuikChange mutagenesis kit (Agilent Technologies). LMG194 host cells (Invitrogen) were used for protein expression. The pWA23h plasmid encoding HO from *Bradyrhizobium ORS278* (hmuO) under control of the rhamnose promoter was cotransformed with a pBAD/His-B plasmid encoding a fluorescent protein[9,35]. Bacterial cells were incubated overnight at 37 °C in RM minimal medium with ampicillin and kanamycin. For initiation of protein expression, 0.002% arabinose and 0.02% rhamnose were added. After growing for 6–8 h at 37 °C, the cells were incubated at 18 °C for 24 h. Proteins were purified with Ni–NTA agarose (Qiagen). Protein was eluted with PBS containing 100 mM EDTA instead of imidazole. Then the samples were desalted with PD-10 desalting columns (GE Healthcare).

Protein characterization in vitro. A FluoroMax-3 spectrofluorometer (Jobin Yvon) was used for recording fluorescence spectra, and a Hitachi U-2000 spectrophotometer was used for absorbance measurements. To determine the extinction coefficients, we calculated a ratio between the maximum absorbance of the main peak at the *Q* band and the side peak at the Soret band and assumed that the extinction coefficient at the Soret band corresponded to 39,900 M^{-1} cm^{-1} (refs. [36,37]). To determine quantum yield, we measured the fluorescence signal of a purified protein in parallel with an equally absorbing Nile blue dye (quantum yield of 0.27)[38] and compared the signal at several dilutions. pH titrations were done with a series of buffers (100 mM sodium acetate, 300 mM NaCl for pH 2.5–5.0 and 100 mM NaH_2PO_4, 300 mM NaCl for pH 4.5–9.0).

To test NIR FPs for their oligomeric state, we performed analytical ultracentrifugation at 20 °C and 58,000 r.p.m. with an Optima XL-I centrifuge (Beckman Coulter) with an AN-60Ti rotor and the absorption optics set to 645 nm. Sednterp v.20120828beta software was used to calculate the partial specific volume of the proteins according to their sequences and the density and viscosity of the buffers. The sedimentation parameters were corrected to standard conditions (*20*,*w*) by using these values. For sedimentation velocity experiments, 350 µl of protein sample and an equal volume of PBS were loaded into two-sector cell assemblies with the protein concentration corresponding to $A_{645} \approx 0.9$. Fifty scans were collected over the course of a centrifuge run. A subset of scans, beginning with those for which a clear plateau was evident between the meniscus and the boundary, was selected for time-derivative analysis in DCDT+ v.2.4.2 software[39,40].

Mammalian plasmids. To test the brightness of NIR FPs, we transiently cotransfected HeLa cells with plasmids encoding EGFP and NIR FP. To construct mammalian expression plasmids, we PCR amplified the respective genes encoding NIR FPs as AgeI–NotI fragments and swapped them with a gene encoding EGFP in the pEGFP-N1 plasmid (Clontech). For example, the miRFP720 gene was swapped with the EGFP gene, thus yielding the pmiRFP720-N1 plasmid. The pmIFP-N1 plasmid was obtained from Addgene (no. 54620).

For protein tagging and labeling of intracellular structures, we swapped a gene encoding miRFP720 with a gene for expression of mTagBFP2 fused either C terminally (for α-tubulin and myosin) or N terminally (for LifeAct, vimentin, LAMP1, H2B and mitochondrial signal)[41]. For C-terminal fusions, we increased the length of the $(SGGGG)_n$ linker to 30 amino acids. For N-terminal fusions, the linker length was unchanged.

For caspase-3 FRET biosensors, fusions of miRFPP670 with miRFP709 and of miRFP670 with miRFP720, containing an 11–amino acid linker with the caspase-3-recognition site (GG*DEVD*GPVAT; the recognition site is marked by italics), were designed. An miRFP670-encoding gene was PCR amplified with primers containing the linker sequence and inserted via the BglII and AgeI restriction sites into the pmiRFP709-N1 and pmiRFP720-N1 plasmids, respectively.

For LOV-TRAP optogenetic experiments, we used pTriEX-N-TOM20-LOV2 and pTriEx-mVenus-Zdk1-VAV2 DHPHC1 (ref. [16]), a gift from K. Hahn (Addgene plasmid nos. 81009 and 81133) (University of North Carolina at Chapel Hill, North Carolina, USA). mTagBFP2[42] was cloned into pTriEX-N-TOM20-LOV2 through overlapping PCR with the following primer pairs: 5′-gcagaattatacttggtataccatggtgggccgcaacagcgcgat-3′ and 5′-tctagatttaaagttcggatcgctg-3′ to amplify the TOM20 fragment; 5′-cagcgatccgaactttaaatctagaatggtgtctaagggcgaagagctga-3′ and 5′-cctatatgcataattaggatccacttccagaaccattcagcttgtgccccagtttgcta-3′ to amplify mTagBFP2; and 5′-gcaattagcaatgtcaggatccttggctactacacttgaacgtattg-3′ and 5′-gcaatgctaatgcatatattctcgagttaaagttcttttgccgcctcatca-3′ to amplify the LOV2 domain. The full-length N-TOM2-mtagBFP2-LOV2 was ligated into the pTriEX-4 backbone via the NcoI and XhoI sites. The full-length WT Trio GEF was a gift from J. van Buul (University of Amsterdam, Amsterdam, Netherlands). Trio DHPH1SH3 (amino acids 1291–1609)[43] was amplified and cloned into pTriEX-mVenus-Zdk1 at the C terminus through overlapping PCR with the following primer pairs: 5′- gcaagattatatgcatattaccatggtgagcaagggcgaggagctgtt-3′ and 5′-agatccacttccgaattccttgtacagctcgtccatgccgaga-3′ to amplify mVenus; 5′- gtacaaggaattcggaagtggatctatggtggataacaaattcaataaag-3′ and 5′-tttaccagatccaccagatccggatccttttggggcctgggcatcgttca-3′ to amplify Zdk1; and 5′- atccggatctggtggatctggtaaaaggaaagagttcataatggctgagct-3′ and 5′-gcattatagaacaattaatctcgagttaggcgtcattgctggagacggagagc-3′ to amplify the TrioDHPH1SH3 fragment. The product was ligated into pTriEX-4 via the NcoI and XhoI sites.

Mammalian cells and transfection. HeLa cells were purchased from the ATCC and were not further authenticated or tested for mycoplasma contamination. HeLa cells were grown in DMEM supplemented with 10% FBS, 0.5% penicillin–streptomycin and 2 mM glutamine (Life Technologies/Invitrogen). For microscopy, cells were cultured in 35-mm glass-bottom Petri dishes with no. 1 coverglasses (MatTek). Transfections of cells with plasmids were performed with either Effectene (Qiagen) or Mirus LT1 (MirusBio) transfection reagents. LinXE cells (HEK293 derivative; mycoplasma tested)[44] were cultured in DMEM supplemented with 10% FBS, 1% Glutamax (Invitrogen) and penicillin (100 IU/ml)–streptomycin (100 IU/ml). Mouse embryonic fibroblasts (MEF/3T3 tet-OFF; mycoplasma tested; Clontech) were cultured in DMEM supplemented with 10% FBS, 1% Glutamax (Invitrogen), penicillin (100 IU/ml)–streptomycin (100 IU/ml) and neomycin-G418 (1 mg/ml), as previously described[15].

Fluorescence of cell suspensions. The fluorescence of uncleaved and cleaved caspase-3 FRET biosensors was measured in transiently transfected HeLa cells 48 h after transfection. To activate biosensor cleavage, we added 2 µM staurosporin to cells grown in six-well plates 6 h before the analysis. Cells were pretreated with 25 µM BV for 24 h before the measurements. Fluorescence spectra of the untreated (uncleaved) and staurosporin-treated (cleaved) cell suspensions were recorded at 610-nm excitation in a 150-µl microcuvette and normalized to acceptor fluorescence at 670 nm for comparison.

Fluorescence microscopy. Live HeLa cells were imaged with an Olympus IX81 inverted epifluorescence microscope 48 h after transfection with miRFP720 fusions. The microscope was equipped with a 200-W metal-halide arc lamp (Lumen220 Pro; Prior), a 100× 1.4-NA oil-immersion objective lens (UPlanSApo; Olympus) and a Cy5.5 filter set (665/45-nm excitation and 725/50-nm emission). The microscope was operated with SlideBook v.4.1 software (Intelligent Imaging Innovations).

To determine protein photostability, unfused NIR FPs were cytoplasmically expressed in HeLa cells and imaged at determined time periods. The obtained raw data were normalized to corresponding absorbance spectra and extinction coefficients of the proteins, the spectrum of the 200-W metal-halide arc lamp and the transmission of the 665/45-nm photobleaching filter. For determining the FRET efficiency in caspase-3-cleavage experiments, 610-nm-wavelength light was used for excitation.

NIR Rac1 biosensor. The previously described single-chain FRET-biosensor for Rac1, based on mCerulean1–circularly permutated monomeric Venus[20,23], was used as the backbone for the new NIR Rac1 biosensor. Briefly, miRFP720 and miRFP670 were synthesized with codon optimization, and conservative point mutations were added to remove internal restriction sites and make the constructs compatible with the original Rac1 biosensor backbone containing a set of unique restriction sites (NcoI, BamHI, HindIII, EagI, NotI, EcoRI and XhoI) and appropriate terminal restriction-site sequences. The miRFP720 was placed in the FP1 position, and miRFP670 was placed in the FP2 position on the basis of the optimization results (Supplementary Fig. 6a). The optimized biosensor backbone contained a miRFP720 as the FRET acceptor; two tandem codon-optimized[23] PBDs from PAK1 (amino acid residues 70–149) to achieve autoinhibitory regulation, which were separated by a structurally optimized linker (GSGGPPGSGGSG), an unstructured linker (L1, 58 amino acid residues) of optimized length based on a previously described design[45]; miRFP670 as the FRET donor; an optimized 10–amino acid linker (GSGSGSGGEL; L2); and a full-length WT Rac1 (Fig. 2a). The second PBD contained H83D and H86D point mutations to render it unable to bind to active GTPase. The synonymous modification[22] was applied to the two PBD domains and repeating units within linker 1 to prevent homologous recombination and stabilize expression. The resulting biosensor construct was cloned into the pTriEX-4 backbone (Novagen) via the NcoI and XhoI sites. For the stable/inducible incorporation of biosensor into the cellular genome, the pRetro-X system was used. Biosensor cDNA cassette was cloned into the pRetro-X-Hygro and pRetro-X-Puro backbones through the Gateway cloning technique (Invitrogen) according to the manufacturer's protocol. For double-positive biosensor transductants, MEFs stably and inducibly expressing the RhoA biosensor[15] or Rac1–GDI biosensor[2] were transduced with retrovirus containing the expression cassette for the NIR Rac1 biosensor under the control of a tetracycline-inducible promoter, but with hygromycin resistance. Methods for production of virus, transduction, selection and biosensor induction were as described previously[46].

Fluorometric characterization of the NIR Rac1 biosensor. Characterization of the biosensor response was performed in LinXE cells (HEK293T derivative) through transient overexpression of WT or mutant versions of the biosensor, with or without the upstream regulators, as described previously[15]. Briefly, LinXE cells were plated on poly-L-lysine (Sigma)-coated six-well plates overnight at 1.25×10^6 cells/well, then transfected the next day with Lipofectamine 2000 (Invitrogen) according to the manufacturer's protocol. Biosensors were cotransfected at ratios of 1:4 with GDI, 1:4 with GAP or 1:(1–4) with GEFs. The transfection solution additionally contained 25 µM BV. 48 h after transfection, cells were washed in PBS, briefly trypsinized and resuspended in cold PBS, the live-cell suspension was placed into a cuvet, and fluorescence emission spectra were measured with a spectrofluorometer (Horiba-Jobin-Yvon Fluorolog-3MF2). The fluorescence emission spectra were obtained by exciting the specimen with 600-nm-wavelength light, and the emission fluorescence was scanned between 640 and 750 nm. The background fluorescence reading of cells containing an empty vector was used to measure light scatter and autofluorescence and was subtracted from the data. The resulting spectra were normalized to the peak miRFP670 emission intensity at 670 nm to generate the final ratiometric spectra.

NIR-Rac1-biosensor pulldown experiments. LinXE cells were plated at a density of 1.25×10^6 cells on poly-L-lysine-coated six-well plates. The next day, cells were transfected with Lipofectamine 2000 (Invitrogen) according to the manufacturer's protocol. 24 h later, the cells were lysed in a buffer containing 1% NP-40, 20 mM Tris, 300 mM NaCl, pH 8.0, 1 mM PMSF and protease-inhibitor cocktail (Sigma). Lysates were clarified by centrifugation at 14,000 r.p.m. for 10 min at 4 °C. After removal of an 'input' fraction, lysates were incubated with PAK1–PBD beads[47] for 1 h at 4 °C with rotation. Samples were washed three times in lysis buffer, resuspended in final sample buffer and analyzed by western blotting[20].

Western blotting. Cell lysates were resolved on 10% SDS–polyacrylamide gels. PVDF membranes were used for blotting. Primary-antibody incubations were performed overnight at 4 °C (1:1,000 dilution). Secondary fluorescently conjugated antibody (LiCor; 926-32210; goat anti-mouse IRDye800CW) was diluted 1:20,000 and incubated for 1 h at room temperature. Immunoblots were recorded with an Odyssey Imager (LiCor). The primary antibodies used were anti-β-actin (Santa Cruz Biotechnology; sc-69879 clone AC-15) and anti-Rac1 (MilliporeSigma 05-389; clone 23A).

Live-cell multiplexed FRET imaging. On the day of the experiment, MEF cells expressing the biosensors were plated at 4.5×10^4 cells per well in standard growth medium containing 25 µM BV onto 25-mm round no. 1.5 coverslips (Warner Instruments) previously coated with 10 µg/ml fibronectin (Sigma) in Dulbecco's PBS for 1 h at room temperature. Cells were time-lapse imaged beginning 2–3 h after plating. Cells were imaged in Ham's F-12K medium without phenol red (Crystalgen), sparged with argon gas to remove dissolved oxygen, and supplemented with 3% FBS, 10 mM HEPES, Oxyfluor reagent at 1:100 dilution (Oxyrase) and 10 mM DL-lactate (Sigma). The imaging medium did not contain exogenous BV during experiments. Cells were imaged at 37 °C in a closed imaging chamber[48]. We used standard wide-field microscopy in our live-cell FRET experiments, as described previously[49].

Biosensor readouts were measured in cells with a custom Olympus IX81-ZDC microscope optimized for FRET[48]. Metamorph v.7.8.13 (Molecular Devices) was used to perform image acquisition. For live-cell imaging, images were acquired through a 40×-magnification objective lens (Olympus UIS DIC, 40×, 1.4 NA) with 2 × 2 camera binning, by using a custom microscope capable of simultaneous acquisition of FRET (mCerulean–mVenus FRET) and mCerulean emissions through two Coolsnap ES2 cameras (Photometrics) mounted onto the side camera port via an optical beam splitter containing a T505LPXR mirror, ET480/40M for mCerulean emission and ET535/30M for mVenus FRET emission (Chroma Technology). The microscope's main body prism was replaced with a T555LPXR mirror (Chroma Technology) to allow for splitting of longer wavelengths to the bottom mounted camera port. A third camera (Coolsnap HQ2; Photometrics) was mounted on the bottom port of the microscope via a filter wheel and used to acquire DIC and miRFP670 and miRFP720 FRET channels sequentially. The associated error due to motion artifacts at the leading edge (6.36 ± 2.6 nm/s (mean ± s.d.)) for the control condition in these MEF cells (calculated during morphodynamic analysis)[1] translated to, on average, 63.6 ± 26 nm positional uncertainty within the 10-s time interval of an acquisition cycle. This result was within the resolution limit of the acquisition condition, with calibrated pixel dimensions at the image plane of 309 nm × 309 nm. In the side-port dual-camera system, the relative intensities between the FRET and mCerulean channels were balanced by inclusion of a neutral density filter in the FRET channel (ND 0.2 for the RhoA biosensor; ND 0.1 for the Rac1–GDI biosensor), so that the ranges of brightness in both channels were similar to each other. Illuminations were all from a 100-W mercury arc-lamp source. For mCerulean–mVenus FRET, cells were illuminated via an ET436/20X band-pass filter (Chroma Technology). For miRFP670–miRFP720 FRET, cells were illuminated with an ET628/32X band-pass filter (Chroma Technology). For the emissions, an ET480/40M and ET535/30M filter pair was used for mCerulean–mVenus FRET (Chroma Technology), and an FF684/24 (Semrock) and FF794/160 (Semrock) filter pair was used for miRFP670 and miRFP720 FRET imaging.

All image channels were aligned before ratiometric calculations through pixel-by-pixel matching using a priori calibration and nonlinear coordinate transformation to achieve registration, as previously described[49]. Metamorph v.7.8.13 (Molecular Devices) and Matlab (Mathworks) software were used to perform image processing and data analysis. Image processing included flat-field correction, background subtraction, camera-noise subtraction, nonlinear coordinate transformation, threshold masking, ratio calculations and correction for photobleaching, as described previously[49]. The detailed optical specifications for the microscope used here have been described elsewhere[48]. For imaging of biosensors, we adjusted the camera acquisition-time duration by targeting to fill approximately 80% of the total digitization range of the charge-coupled-device circuitry to maximize the dynamic range, by using excitation intensities of 0.4–1.0 mW at the specimen plane.

Morphodynamic mapping and cross-correlation analysis. Morphodynamic-mapping and cross-correlation methods were as described previously[1]. The primary assumption at the core of this analysis is that the relationship between GTPase activation and the movements of the cell edge during constitutive protrusion–retraction cycles is preserved anywhere within the edge of a single cell and among all cells within a given population[1]. This assumption allowed us to evaluate the behavior of a small segment of an edge as an independent sampling entity and then average such measurements from many segments to perform cross-correlational analyses between multiple measurement parameters. Briefly, the analysis algorithm first tracks the leading-edge motion through a previously described method[1]. After the leading-edge positions are defined as a function of time from a time-lapse series, measurement-window segments are defined along the cell edge to measure the parameters of interest within single window-segment entities. In this work, we measured two biosensor activities and the cell-edge velocity in sampling-window segments of 0.9 × 1.8 µm constructed along the leading edges of cells, and tracked the cell-edge motion during complete protrusion–retraction cycles. We have previously determined that this particular measurement-window dimension was diffusion limited (minimal diffusional mixing of membrane-bound components between adjacent windows, assuming a two-dimensional, membrane-bound diffusion constant: at the cell edge, there would be very little cytoplasm present) within the time interval of imaging (10 s per image), the objective magnification and the pixel dimension of the imaging system used[1]. Thus, by maintaining such a diffusion-limited sampling dimension, we ensured that the readout from individual measurement-window segments could be treated as independent sampling entities[1]. By constructing many individual, independent measurement-window segments along edges in a number of cells from a given population, we achieved sufficient statistical power to determine the significance of localization of activities in space and time, as in our previous studies[1,2,23]. Next, measurement-window segments were moved away from the leading edge in 0.9-µm increments to measure two biosensor readouts at successively distal regions away from the edge. The extent of coupling between changes in the two biosensor activity readouts was determined with the cross-correlation function *xcov* in Matlab, and Pearson's correlation coefficient was used to determine the strength of coupling of two biosensor readouts. In addition to determining the spatial coupling, this approach also measures the temporal relationship between the two measured biosensor readouts. In this work, we analyzed $n = 1,250$ window segments from 16 cells for the control RhoA–Rac1 multiplex measurements; $n = 990$ window segments from 18 cells for ROCK-inhibited RhoA–Rac1 measurements; and $n = 827$ window segments from 10 cells for Rac1–GDI binding and Rac1 activity measurements. The numbers of individual window segments constructed and total number of cells analyzed per cell population/condition were similar to those in previous studies[1,2,23]. The resulting cross-correlation functions were compiled and analyzed with the 2,000× bootstrapping of the smooth-spline fit functions from the individual window segments to determine the 95% CIs. The autocorrelation function of the leading-edge-protrusion velocities was used as a measure to indicate the periodicity of the intrinsic protrusion–retraction cycles[1]. This analysis indicated that in all cases analyzed, the expression of two biosensors did not alter the basic protrusion periodicity from that of the previously published RhoA-biosensor MEF cell line[15], imaged under current conditions (Supplementary Fig. 10). The morphodynamic analysis as used in this work does not separately parse out the behavior of biosensor activities as a function of edge protrusion or retraction. Instead, it takes the protrusion–retraction as single cycles and produces global cross-correlation functions taking into account many cycles of these processes. Thus, we imaged steady-state cells, taking advantage of the continuous cycles of protrusion–retraction that occur at random locations along the cell edge at steady state. This measurement enabled us to sample many iterations of protrusion–retraction behaviors and build a statistically robust cross-correlation function between the two signaling nodes. Future research directions, although beyond the scope of this present work, could include parsing out the GTPase behaviors during protrusion versus retraction, as well as analyzing the correlative coupling of signaling nodes during acute exogenous stimulations.

In relation to the effect of increasing cell volume in regions away from the leading edge and how cytoplasmic biosensor accumulation could influence the cross-correlation analysis, we expect that the positive cross-correlation observed between Rac1 activity and Rac1–GDI binding at the region adjacent to the leading edge (Fig. 4) reflects their functional importance, as opposed to a random response caused by changes in cytoplasmic volume. Because wide-field imaging was used, an increase in cytoplasmic volume could have increased the FRET signal from the cytoplasmic accumulation of Rac1–GDI biosensor in complex with the cytoplasmic

GDI. In contrast, the NIR Rac1 biosensor could have indicated decreased activity from the volume dilution effect, in which low FRET signal from the inactive and cytoplasmic-partitioned NIR Rac1 biosensor may have diluted the high FRET signal from active biosensor in the plasma membrane (this dilution effect has previously been modeled by Spiering et al.[49]). In such a situation involving opposing signal modulation, either a negative cross-correlation would be expected, or no correlation would be observed if only one of these volume-associated issues predominated. Thus, our observation of positive cross-correlation at this location suggests binding of more Rac1 by GDI (and accumulation of Rac1–GDI complex in increased cytoplasmic volume) as well as activation of Rac1 at this location.

Optogenetic experiments with LOV-TRAP. In experiments using the LOV-TRAP[16] system to target the Trio GEF catalytic domain for Rac1 activation, MEF cells stably and inducibly expressing the NIR Rac1 biosensor were transfected with the required components. Briefly, MEFs were induced to undergo biosensor expression 48 h before the experiment in the presence of 25 μM BV, through a previously described biosensor-induction method[46]. 24 h after the induction, cells were briefly trypsinized, pooled and seeded onto six-well plates at a density of 1×10^5 cells/well, and transfected with Fugene 6 reagent (Roche) according to the manufacturer's protocol. A DNA ratio of 10:1 pTriEX-N-TOM20-mtagBFP2-LOV2 to pTriEX-mVenus-Zdk1-TrioDHPH1SH3 was used. The plasmids were premixed at this ratio before the transfection mixture was made according to previously published protocols[16]. Cells were imaged for 24 h after the transfection. The imaging system was set up to enable whole-field photoactivation with 457-nm light that was pulsed every 10 s (4 s on, 6 s off). Cells positive for LOV-TRAP expression were visualized and identified with mTagBFP2/mVenus. Cells were then imaged without photoactivation for 31 frames at a 10-s interval per frame. The photoactivation sequence was initiated between frames 31 and 32, and continued at 10-s intervals for 30 additional frames concurrent with the biosensor measurements at the same interval. Data were acquired for an additional 30 frames after the end of the photoactivation sequence at the same acquisition intervals for a total of 90 frames from beginning to end.

NIR kinase biosensors. To clone the NIR JNKAR and NIR AKAR biosensors, we used the pJNKAR1EV-NES and pAKAR3EV-NES plasmids[33], respectively, which were kindly provided by K. Aoki (Kyoto University, Kyoto, Japan). YPet and ECFP in the original AKAR and JNKAR constructs were exchanged for miRFP670 and miRFP720 via the EcoRI/XhoI and NotI/XbaI restriction sites, respectively. Fragments encoding NIR sensors were excised with EcoRI/SalI restriction endonucleases and inserted into the pcDNA3.1 plasmid.

For imaging of NIR AKAR and NIR JNKAR, HeLa cells were seeded at a density of 1×10^5 cells/coverslip in wells of six-well plates onto 25-mm round coverslips treated with 10 μg/ml fibronectin (Sigma) in PBS for 1 h at room temperature. Cells were transfected with Fugene 6 reagent (Roche) according to the manufacturer's protocol. 6 h after addition of the transfection mixture to cells, the medium was supplemented with 25 μM BV. 24 h after the transfection, cells were serum starved for 8 h in medium containing 0.1% BSA without exogenous BV. At the end of starvation, cells were mounted in a live-cell imaging chamber atop a microscope stage and imaged at 37 °C under mineral oil. Cells were time-lapse imaged at 2-min intervals, and DIC and NIR-FRET/donor image pairs were acquired at each time point. After the baseline signal response was established for 10 min in the absence of stimuli, stimulations were performed by addition of 1 mM dibutyryl cAMP or 1 μg/ml anisomycin, for AKAR and JNKAR, respectively. After the stimulation, time-lapse imaging was performed for an additional 1 h at 2-min intervals. Image processing and analysis of FRET/donor ratio data were performed similarly to the procedures used for the NIR Rac1 biosensor, described above. Although beyond the scope of the present work, further sensor optimization by modulating the dipole coupling angles and changing the lengths and structures of the intramolecular linkers may improve the dynamic range of the sensor response, as demonstrated here for the NIR Rac1 biosensor.

Flow cytometry. Flow cytometry analysis of NIR FPs was performed with a BD LSRII flow cytometer equipped with 488-nm and 640-nm lasers and a set of emission filters. 20,000–50,000 events for each cell type were analyzed. To quantify cell fluorescence, the mean fluorescence intensity of the double-positive population in the NIR channel was divided by the mean fluorescence intensity of the same population in the green channel, thus normalizing the NIR signal to transfection efficiency.

Statistical analysis. All statistical significance based on *P* values was determined with Student's *t* tests. No vertebrate animals were used in this study. No statistical methods were used to predetermine the sample size. No randomization was used. The investigators were not blinded to allocation during experiments and outcome assessment. Statistical tests used are stated in every figure legend with *P* values as appropriate. The data distribution should meet normal distribution requirements. No estimate of variation was performed. No preestablished criteria were used to determine data inclusion or exclusion.

Code availability. All Matlab codes and Metamorph scripts used have been previously published[1,2,49] but are also available from the corresponding authors upon reasonable request.

Reporting Summary. Further information on experimental design is available in the Nature Research Reporting Summary.

Data availability. The data that support the findings of this study are available from the corresponding authors upon reasonable request.

References

35. Piatkevich, K. D., Subach, F. V. & Verkhusha, V. V. Far-red light photoactivatable near-infrared fluorescent proteins engineered from a bacterial phytochrome. *Nat. Commun.* **4**, 2153 (2013).
36. Filonov, G. S. et al. Bright and stable near-infrared fluorescent protein for in vivo imaging. *Nat. Biotechnol.* **29**, 757–761 (2011).
37. Shu, X. et al. Mammalian expression of infrared fluorescent proteins engineered from a bacterial phytochrome. *Science* **324**, 804–807 (2009).
38. Sens, R. & Drexhage, K. H. Fluorescence quantum yield of oxazine and carbazine laser dyes. *J. Lumin.* **24**, 709–712 (1981).
39. Philo, J. S. Improved methods for fitting sedimentation coefficient distributions derived by time-derivative techniques. *Anal. Biochem.* **354**, 238–246 (2006).
40. Stafford, W. F. III. Boundary analysis in sedimentation transport experiments: a procedure for obtaining sedimentation coefficient distributions using the time derivative of the concentration profile. *Anal. Biochem.* **203**, 295–301 (1992).
41. Subach, O. M., Cranfill, P. J., Davidson, M. W. & Verkhusha, V. V. An enhanced monomeric blue fluorescent protein with the high chemical stability of the chromophore. *PLoS One* **6**, e28674 (2011).
42. Subach, O. M. et al. Conversion of red fluorescent protein into a bright blue probe. *Chem. Biol.* **15**, 1116–1124 (2008).
43. van Rijssel, J., Hoogenboezem, M., Wester, L., Hordijk, P. L. & Van Buul, J. D. The N-terminal DH-PH domain of Trio induces cell spreading and migration by regulating lamellipodia dynamics in a Rac1-dependent fashion. *PLoS One* **7**, e29912 (2012).
44. Brunet, J. P. et al. Rotavirus infection induces cytoskeleton disorganization in human intestinal epithelial cells: implication of an increase in intracellular calcium concentration. *J. Virol.* **74**, 10801–10806 (2000).
45. Whitlow, M. et al. An improved linker for single-chain Fv with reduced aggregation and enhanced proteolytic stability. *Protein Eng.* **6**, 989–995 (1993).
46. Hodgson, L., Pertz, O. & Hahn, K. M. Design and optimization of genetically encoded fluorescent biosensors: GTPase biosensors. *Methods Cell Biol.* **85**, 63–81 (2008).
47. Benard, V. & Bokoch, G. M. Assay of Cdc42, Rac, and Rho GTPase activation by affinity methods. *Methods Enzymol.* **345**, 349–359 (2002).
48. Spiering, D. & Hodgson, L. Multiplex imaging of Rho family GTPase activities in living cells. *Methods Mol. Biol.* **827**, 215–234 (2012).
49. Spiering, D., Bravo-Cordero, J. J., Moshfegh, Y., Miskolci, V. & Hodgson, L. Quantitative ratiometric imaging of FRET-biosensors in living cells. *Methods Cell Biol.* **114**, 593–609 (2013).

nature research

Corresponding author(s): Vladislav Verkhusha, Louis Hodgson

☐ Initial submission ☐ Revised version ☒ Final submission

Life Sciences Reporting Summary

Nature Research wishes to improve the reproducibility of the work that we publish. This form is intended for publication with all accepted life science papers and provides structure for consistency and transparency in reporting. Every life science submission will use this form; some list items might not apply to an individual manuscript, but all fields must be completed for clarity.

For further information on the points included in this form, see Reporting Life Sciences Research. For further information on Nature Research policies, including our data availability policy, see Authors & Referees and the Editorial Policy Checklist.

Experimental design

1. Sample size	
Describe how sample size was determined.	No sample-size calculations were performed. Standard N>3 independent experiments were performed for most cases, unless noted in the figure legend.
2. Data exclusions	
Describe any data exclusions.	No data were excluded
3. Replication	
Describe whether the experimental findings were reliably reproduced.	All attempts at replication were successful.
4. Randomization	
Describe how samples/organisms/participants were allocated into experimental groups.	Not applicable, it is not a clinical trial, no animal/human studies involved
5. Blinding	
Describe whether the investigators were blinded to group allocation during data collection and/or analysis.	Not applicable, it is not a clinical trial, no animal/human studies involved

Note: all studies involving animals and/or human research participants must disclose whether blinding and randomization were used.

6. Statistical parameters

For all figures and tables that use statistical methods, confirm that the following items are present in relevant figure legends (or in the Methods section if additional space is needed).

n/a	Confirmed	
☐	☒	The exact sample size (*n*) for each experimental group/condition, given as a discrete number and unit of measurement (animals, litters, cultures, etc.)
☒	☐	A description of how samples were collected, noting whether measurements were taken from distinct samples or whether the same sample was measured repeatedly
☐	☒	A statement indicating how many times each experiment was replicated
☐	☒	The statistical test(s) used and whether they are one- or two-sided (note: only common tests should be described solely by name; more complex techniques should be described in the Methods section)
☒	☐	A description of any assumptions or corrections, such as an adjustment for multiple comparisons
☐	☒	The test results (e.g. *P* values) given as exact values whenever possible and with confidence intervals noted
☐	☒	A clear description of statistics including central tendency (e.g. median, mean) and variation (e.g. standard deviation, interquartile range)
☐	☒	Clearly defined error bars

See the web collection on statistics for biologists for further resources and guidance.

Software

Policy information about availability of computer code

7. Software

Describe the software used to analyze the data in this study.	Previously published codes written in Matlab and in Metamorph scripts were used and referenced in the text. These codes are available by writing to the corresponding authors, as stated in those previous publications. Commercial software: Sednterp v.20120828 beta, DCDT v.2.4.2, FlowJo 7.6.2, Metamorph v.7.8.13.0, and Matlab 2011a were used

For manuscripts utilizing custom algorithms or software that are central to the paper but not yet described in the published literature, software must be made available to editors and reviewers upon request. We strongly encourage code deposition in a community repository (e.g. GitHub). *Nature Methods* guidance for providing algorithms and software for publication provides further information on this topic.

Materials and reagents

Policy information about availability of materials

8. Materials availability

Indicate whether there are restrictions on availability of unique materials or if these materials are only available for distribution by a for-profit company.	No restrictions, materials are available by contacting the corresponding authors and/or commercial sources.

9. Antibodies

Describe the antibodies used and how they were validated for use in the system under study (i.e. assay and species).	anti-Rac1: MilliporeSigma 05-389, clone 23A, lot#2586803, 1:1000 dilution. anti-beta-actin: Santa Cruz Biotechnology; sc-69879 clone AC-15, lot#D1217, 1:1000 dilution. Goat-anti-Mouse secondary antibody-IRDye800: LiCor; 926-32210, lot#C40213-01, 1:20000 dilution. All antibodies were sourced commercially.

10. Eukaryotic cell lines

a. State the source of each eukaryotic cell line used.	HeLa: ATCC, MEF3T3: Clontech, and LinXE: Dr. Klaus Hahn (UNC-Chapel Hill)
b. Describe the method of cell line authentication used.	HeLa cell line was obtained from ATCC and was not additionally authenticated. ATCC authenticates cell lines using STR analysis according to the product specification webpage. MEF/3T3 tet-OFF cell line was purchased from Clontech and were not additionally authenticated. According to Clontech, MEF/3T3 Tet-Off Cells were transiently transfected by electroporation with pTRE2-Luc. Luciferase activity in the presence and absence of 1 µg/ml doxycycline (Cat. No. 631311) was measured 48 hr later as described in the Tet Systems User Manual. Induction was observed to be at least 80-fold when cells were grown in medium containing Clontech's Tet System Approved FBS. This indicates that cell line contains the tet-inducible component that is integrated into the genome. LinXE cell line was obtained from Dr. Klaus Hahn (UNC-Chapel Hill) and were not additionally authenticated.
c. Report whether the cell lines were tested for mycoplasma contamination.	HeLa cell line was obtained from ATCC and were not additionally tested for mycoplasma. LinXE and MEF/3T3 tet-OFF lines were tested for mycoplasma contamination and were negative based on the PCR assay performed in house.
d. If any of the cell lines used are listed in the database of commonly misidentified cell lines maintained by ICLAC, provide a scientific rationale for their use.	No commonly misidentified cell lines were used.

Animals and human research participants

Policy information about studies involving animals; when reporting animal research, follow the ARRIVE guidelines

11. Description of research animals

Provide details on animals and/or animal-derived materials used in the study.	No animals were used in the study

Policy information about studies involving human research participants

12. Description of human research participants

Describe the covariate-relevant population characteristics of the human research participants.	No humans subjects were used in the study

nature research

Corresponding author(s): Vladislav Verkhusha, Louis Hodgson

☐ Initial submission ☐ Revised version ☒ Final submission

Flow Cytometry Reporting Summary

Form fields will expand as needed. Please do not leave fields blank.

Data presentation

For all flow cytometry data, confirm that:

☐ 1. The axis labels state the marker and fluorochrome used (e.g. CD4-FITC).

☐ 2. The axis scales are clearly visible. Include numbers along axes only for bottom left plot of group (a 'group' is an analysis of identical markers).

☐ 3. All plots are contour plots with outliers or pseudocolor plots.

☐ 4. A numerical value for number of cells or percentage (with statistics) is provided.

Methodological details

5. Describe the sample preparation.	HeLa cells from ATCC
6. Identify the instrument used for data collection.	BD LSRII
7. Describe the software used to collect and analyze the flow cytometry data.	BD FACS Diva 8.0.1; FlowJo 7.6.2
8. Describe the abundance of the relevant cell populations within post-sort fractions.	Not applicable
9. Describe the gating strategy used.	Initial gates - FSC-A/SSC-A to discriminate cells from debris; then cells were gated in FSC-W/FSC-A to discriminate single cells; then cells were gated in SSC-W/SSC-A to discriminate live cells. Resulted population were analyzed on SSC-A/FITC-A plot to find cells expressing EGFP and NIR-FP. Non-transfected cells were used for selecting negative population.

Tick this box to confirm that a figure exemplifying the gating strategy is provided in the Supplementary Information. ☐